Estimation of elastic constants for HTI media using Gauss-Newton and full-Newton multiparameter full-waveform inversion

GEOPHYSICS, VOL. 81, NO. 5 (SEPTEMBER-OCTOBER 2016); P. R275–R291, 17 FIGS.
10.1190/GEO2015-0594.1

Estimation of elastic constants for HTI media using Gauss-Newton and full-Newton multiparameter full-waveform inversion

Wenyong Pan[1], Kristopher A. Innanen[1], Gary F. Margrave[1], Michael C. Fehler[2], Xinding Fang[2], and Junxiao Li[1]

ABSTRACT

In seismic full-waveform inversion (FWI), subsurface parameters are estimated by iteratively minimizing the difference between the modeled and the observed data. We have considered the problem of estimating the elastic constants of a fractured medium using multiparameter FWI and modeling naturally fractured reservoirs as equivalent anisotropic media. Multiparameter FWI, although promising, remains exposed to a range of challenges, one being the parameter crosstalk problem resulting from the overlap of Fréchet derivative wavefields. Parameter crosstalk is strongly influenced by the form of the scattering pattern for each parameter. We have derived 3D radiation patterns associated with scattering from a range of elastic constants in general anisotropic media. Then, we developed scattering patterns specific to a horizontal transverse isotropic (HTI) medium to draw conclusions about parameter crosstalk in FWI. Bare gradients exhibit crosstalk, as well as artifacts caused by doubly scattered energy in the data residuals. The role of the multiparameter Gauss-Newton (GN) Hessian in suppressing parameter crosstalk is revealed. We have found that the second-order term in the multiparameter Hessian, which is associated with multiparameter second-order scattering effects, can be constructed with the adjoint-state technique. We have examined the analytic scattering patterns for HTI media with a 2D numerical example. We have examined the roles played by the first- and second-order terms in multiparameter Hessian to suppress parameter crosstalk and second-order scattering artifacts numerically. We have also compared the multiparameter GN and full-Newton methods as methods for determining the elastic constants in HTI media with a two-block-layer model.

INTRODUCTION

Naturally fractured reservoirs are common and play an important role in current hydrocarbon production (Nelson, 1985). Fracture properties are among the most valuable data for reservoir characterization. The influence of fractures/cracks in a geologic medium on the seismic response can be modeled via an equivalent anisotropic solid and the associated elastic stiffness coefficients (Hudson, 1981; Schoenberg, 1983). For transverse isotropy with a horizontal symmetry axis (horizontal transverse isotropic [HTI] media), the simplest azimuthal anisotropic model for describing vertical cracks, reflection seismic signatures can be described by five independent elastic constants (Rüger, 1997; Tsvankin, 1997a, 1997b). In reflection seismology, most current methods for estimating fracture properties focus on amplitude and traveltime methods (Thomsen, 1988; Tsvankin, 1997b). Full-waveform inversion (FWI) methods make maximal use of wavefield information to estimate subsurface properties by iteratively minimizing the difference between the modeled and observed data (Lailly, 1983; Tarantola, 1984; Virieux and Operto, 2009; Warner et al., 2013). In this research, we consider the problem of estimating elastic constants in anisotropic media using multiparameter FWI.

Much current FWI research emphasizes reconstruction of the P-wave velocity and associated core problems, such as cycle skipping (Ma and Hale, 2012; Warner and Guasch, 2014; Wu et al., 2014). Inverting multiple parameters using multiparameter FWI has also, however, received increased attention in recent years though it is a more challenging task. Involving several parameters increases the nonlinearity of the inversion process and also introduces parameter crosstalk, the conflation of the influence of one physical property on

Manuscript received by the Editor 1 November 2015; revised manuscript received 21 March 2016; published online 26 July 2016.
[1]University of Calgary, Department of Geoscience, CREWES Project, Calgary, AB, Canada. E-mail: wpan@ucalgary.ca; k.innanen@ucalgary.ca; margrave@ucalgary.ca; li.junxiaoo@uclagary.ca.
[2]Massachusetts Institute of Technology, Earth Resources Laboratory, Cambridge, Massachusetts, USA. E-mail: fehler@mit.edu; fangxinding@gmail.com.

the data with another (Operto et al., 2013; Prieux et al., 2013; Baumstein, 2014; Innanen, 2014a; Métivier et al., 2015; Oh et al., 2015). Parameter crosstalk is strongly present in steepest-descent method, wherein updates in each parameter proceed with no accounting for the multiparameter character of the problem. However, even when the multiparameter character of a system is properly included in a FWI update, crosstalk persists if the wavefield variation caused by one parameter is similar to that caused by another physical parameter. Hence, the Fréchet derivative wavefields associated with different physical parameters are crucial to understand the parameter crosstalk problem in multiparameter FWI. Tarantola (1986) originally introduces the use of scattering patterns for crosstalk analysis of different parameter classes in isotropic and elastic FWI. Inversion sensitivity analysis in anisotropic media has been studied by many researchers (Gholami et al., 2013a, 2013b; Alkhalifa and Plessix, 2014; Kamath and Tsvankin, 2014; Podgornova et al., 2015).

Multiparameter Hessian in FWI is a square and symmetric matrix with a block structure. It carries more information than a single-parameter Hessian. Within the approximate Hessian associated with a multiparameter Gauss-Newton (GN) update, off-diagonal blocks measure correlation of Fréchet derivative wavefields with respect to different physical parameters. They act to mitigate the coupling effects between these parameters (Operto et al., 2013). Innanen (2014b), for instance, shows that the diagonal elements internal to the off-diagonal blocks suppress crosstalk in precritical reflection FWI in a manner consistent with amplitude variation with offset inversion and linearized inverse scattering.

The gradient vector is also known to be contaminated by the second-order scattered energy in the data residuals. Pratt et al. (1998) discuss and analyze the second-order term in the single-parameter Hessian, which accounts for the second-order scattering effects. This term becomes important when the data residuals or the second-order scattered energy are very strong (Métivier et al., 2014). Incorporating this second-order term can eliminate the second-order scattering artifacts in the gradient vector. This term in a multiparameter Hessian becomes more complex. The second-order partial derivative wavefields can be caused by the perturbations of different physical parameters. The second-order term predicts the change in the gradient due to the multiparameter second-order nonlinear effects. Here, we include this second-order term in the multiparameter Hessian, using an adjoint-state method to calculate it (Pratt et al., 1998). Involving the first- and second-order terms in the multiparameter Hessian for preconditioning the gradient is known as the full-Newton (FN) method.

In this research, analytic expressions for the 3D scattering patterns of the elastic constants in general anisotropic media are derived. Then, we illustrate the scattering patterns of elastic constants in a specific HTI medium for parameter crosstalk analysis. Furthermore, we numerically examine the ability of the multiparameter approximate Hessian to suppress parameter crosstalk for HTI elastic constants inversion. Pratt et al. (1998) calculate the second-order term in single-parameter Hessian using an adjoint-state method. In this paper, we show that the second-order term in multiparameter Hessian associated with multiparameter second-order scattering effects can also be constructed with the adjoint-state technique.

The paper is organized as follows. First, we review the theories for the forward modeling problem and FWI. Then, we discuss the parameter crosstalk difficulty in multiparameter FWI. The analytic expressions of 3D scattering patterns for the elastic constants in general anisotropic media are derived. The physical interpretations of the first- and second-order terms in multiparameter Hessian are given. Their roles in suppressing parameter crosstalk and second-order scattering effects are revealed. We also describe how to construct the second-order term using the adjoint-state method. In the numerical modeling section, we examine the analytic and numerical scattering patterns of the elastic constants for parameter crosstalk analysis. Several numerical examples are presented to illustrate the role of multiparameter Hessian in mitigating parameter crosstalk and second-order scattering artifacts. The GN and FN multiparameter FWI are finally applied on a two-block-layer model for comparison.

THEORY AND METHODS

In this section, we first review the basic principles of forward modeling in anisotropic media and FWI. We then introduce the issue of parameter crosstalk for inverting the elastic constants in HTI media using multiparameter FWI. We derive the 3D scattering patterns for elastic constants in general anisotropic media. The roles of multiparameter Hessian in suppressing parameter crosstalk and second-order scattering effects are revealed.

Forward modeling problem

In reflection seismology, the wavelengths of seismic waves are typically much larger than the fracture size. When considering that the fractures are closely spaced and parallel, the finite fracture spacings and their detailed spatial distributions can be neglected. The fractured medium can be replaced by effective anisotropic solids. The reflection seismic signatures are associated with the elastic stiffness coefficients c_{IJ} through the equation of motion in general anisotropic media (Hudson, 1981; Schoenberg, 1983). With Einstein summation notation, it can be expressed as

$$\frac{\partial \sigma_{ij}}{\partial x_j} + f_i = \rho \frac{\partial^2 u_i}{\partial t^2}, \tag{1}$$

where $u_i(\mathbf{x}, t)$ indicates the ith component of the particle displacement at Cartesian coordinate position $\mathbf{x} = (x, y, z)$ and time t, $f_i(\mathbf{x}_s)$ is the source term at position $\mathbf{x}_s$, ρ is the density, and σ_{ij} denotes the stress tensor, which can be defined using Hooke's law,

$$\sigma_{ij} = c_{ijkl} e_{kl}, \tag{2}$$

where c_{ijkl} indicates the elastic modulus tensor, $e_{kl} = 1/2((\partial u_k/\partial x_l) + (\partial u_l/\partial x_k))$ is the strain tensor, and the subscripts i, j, k, and l take on the values of 1, 2, and 3. Thus, 81 elastic constants are required to characterize the elasticity of the medium. Because the symmetry of the stress and strain tensors, only 21 elastic stiffness coefficients are independent and the $3 \times 3 \times 3 \times 3$ tensor c_{ijkl} can be represented more compactly using 6×6 symmetric matrix c_{IJ} following the Voigt recipe for indexes, where I and J range from 1 to 6 (Crampin, 1984; Tsvankin and Grechka, 2011).

Models containing parallel vertical fractures are equivalent to HTI media, which can be characterized by five independent elastic constants, c_{33}, c_{55}, c_{11}, c_{13}, and c_{44}. We extract the x-z plane with zero azimuth angle from 3D geometry, which forms the simplified 2D HTI model described by four elastic constants (c_{33}, c_{55}, c_{11}, and c_{13}). Numerical solutions of the wavefields are calculated using an

explicit finite-difference method with fourth-order accuracy in space and second-order accuracy in time (Virieux, 1986; Levander, 1988). A nonsplitting perfectly matched layer boundary condition is applied on all boundaries of the model (Berenger, 1994; Wang and Tang, 2003).

GN and FN FWI

FWI estimates the subsurface parameters through an iterative process by minimizing the difference between the synthetic data $\mathbf{u}_{\text{syn}}$ and observed data $\mathbf{u}_{\text{obs}}$ (Lailly, 1983; Tarantola, 1984; Virieux and Operto, 2009). The misfit function Φ is formulated in a least-squares form,

$$\Phi(\mathbf{m}) = \frac{1}{2}\sum_{\mathbf{x}_s}\sum_{\mathbf{x}_g}\sum_{\omega}\|\mathbf{u}_{\text{obs}}(\mathbf{x}_g,\mathbf{x}_s,\omega) - \mathbf{u}_{\text{syn}}(\mathbf{x}_g,\mathbf{x}_s,\omega)\|^2, \tag{3}$$

where $\mathbf{m}$ indicates the model parameter, $\mathbf{x}_s$ and $\mathbf{x}_g$ denote the positions of sources and receivers, respectively, ω is the angular frequency, and $\|\cdot\|$ means the $\ell 2$ norm. Note that we implement the algorithms in the time domain, whereas the notations are expressed in the frequency domain for sake of compactness. The Newton optimization approach is developed based on the second-order Taylor-Lagrange expansion of the misfit function Φ:

$$\Phi(\mathbf{m}+\Delta\mathbf{m}) \approx \Phi(\mathbf{m}) + \mathbf{g}^{\dagger}\Delta\mathbf{m} + \frac{1}{2}\Delta\mathbf{m}^{\dagger}\mathbf{H}\Delta\mathbf{m}, \tag{4}$$

where the symbol $\dagger$ represents transpose, $\Delta\mathbf{m}$ is the search direction, and $\mathbf{g} = \nabla_{\mathbf{m}}\Phi(\mathbf{m})$ and $\mathbf{H} = \nabla_{\mathbf{m}}\nabla_{\mathbf{m}}\Phi(\mathbf{m})$ indicate gradient and Hessian, respectively. To minimize the quadratic approximation of the misfit function, the model update at the $(n+1)$th iteration can be written as the sum of the model at the nth iteration and model perturbation $\Delta\mathbf{m}$:

$$\mathbf{m}_{n+1} = \mathbf{m}_n + \mu_n\Delta\mathbf{m}_n, \tag{5}$$

where μ_n is the step length, a scalar constant calculated through a line search method or a trust-region procedure (Gauthier et al., 1986; Pica et al., 1990; Nocedal and Wright, 2006). Within a Newton optimization framework, the search direction $\Delta\mathbf{m}$ is the solution of the Newton linear system:

$$\mathbf{H}_n\Delta\mathbf{m}_n = -\mathbf{g}_n. \tag{6}$$

Gradient is the first-order partial derivative of the misfit function with respect to model parameter. It indicates the direction in which the misfit function is increasing most rapidly (Pratt et al., 1998). It can be constructed by zero-lag correlation between the Fréchet derivative wavefield with complex conjugate of the data residuals $\Delta\mathbf{d}$:

$$\begin{aligned}\mathbf{g}(\mathbf{x}) &= \nabla_{\mathbf{m}(\mathbf{x})}\Phi(\mathbf{m})\\ &= -\sum_{\mathbf{x}_g}\sum_{\mathbf{x}_s}\sum_{\omega}\Re\left(\frac{\partial\mathbf{u}^{\dagger}(\mathbf{x}_g,\mathbf{x}_s,\omega)}{\partial\mathbf{m}(\mathbf{x})}\Delta\mathbf{d}^{*}(\mathbf{x}_g,\mathbf{x}_s,\omega)\right),\end{aligned} \tag{7}$$

where the $*$ symbol represents the complex conjugate, $\Re(\cdot)$ denotes the real part, and $\partial\mathbf{u}(\mathbf{x}_g,\mathbf{x}_s,\omega)/\partial\mathbf{m}(\mathbf{x})$ is known as the Fréchet derivative wavefield or Jacobian matrix. Recalling the generalized Helmholtz equation in anisotropic media with matrix form (Marfurt, 1984),

$$\mathbf{L}(\mathbf{m},\omega)\mathbf{u}(\mathbf{x}_g,\mathbf{x}_s,\omega) = \mathbf{f}_s(\omega), \tag{8}$$

where $\mathbf{L}(\mathbf{m},\omega)$ is the complex impedance matrix, $\mathbf{u}(\mathbf{x}_g,\mathbf{x}_s,\omega)$ is the pressure wavefield vector, and $\mathbf{f}_s(\omega)$ is the source term. Taking the partial derivative with respect to the model parameter on both sides of equation 8 gives

$$\mathbf{L}(\mathbf{m},\omega)\frac{\partial\mathbf{u}(\mathbf{x}_g,\mathbf{x}_s,\omega)}{\partial\mathbf{m}(\mathbf{x})} = -\frac{\partial\mathbf{L}(\mathbf{m},\omega)}{\partial\mathbf{m}(\mathbf{x})}\mathbf{u}(\mathbf{x}_g,\mathbf{x}_s,\omega). \tag{9}$$

Equation 9 describes the propagation of scattered wavefield due to the perturbation of model parameter $\mathbf{m}(\mathbf{x})$. The interaction of incident wavefield with the model perturbation serves as the first-order virtual source $\tilde{\mathbf{f}}_s(\mathbf{x},\omega)$:

$$\tilde{\mathbf{f}}_s(\mathbf{x},\omega) = -\frac{\partial\mathbf{L}(\mathbf{m},\omega)}{\partial\mathbf{m}(\mathbf{x})}\mathbf{u}(\mathbf{x}_g,\mathbf{x}_s,\omega). \tag{10}$$

Isolating the Fréchet derivative wavefield on the left side of equation 9 yields (Shin et al., 2001; Virieux and Operto, 2009)

$$\frac{\partial\mathbf{u}(\mathbf{x}_g,\mathbf{x}_s,\omega)}{\partial\mathbf{m}(\mathbf{x})} = -\mathbf{L}^{-1}(\mathbf{m},\omega)\frac{\partial\mathbf{L}(\mathbf{m},\omega)}{\partial\mathbf{m}(\mathbf{x})}\mathbf{u}(\mathbf{x}_g,\mathbf{x}_s,\omega). \tag{11}$$

Inserting equation 11 into equation 7 gives

$$\begin{aligned}\mathbf{g}(\mathbf{x}) = \sum_{\mathbf{x}_g}\sum_{\mathbf{x}_s}\sum_{\omega}\Re\Bigg(&\mathbf{u}^{\dagger}(\mathbf{x}_g,\mathbf{x}_s,\omega)\\ &\times\frac{\partial\mathbf{L}^{\dagger}(\mathbf{m},\omega)}{\partial\mathbf{m}(\mathbf{x})}\mathbf{L}^{-1}(\mathbf{m},\omega)\Delta\mathbf{d}^{*}(\mathbf{x}_g,\mathbf{x}_s,\omega)\Bigg),\end{aligned} \tag{12}$$

where $(\mathbf{L}^{-1})^{\dagger}$ is replaced with $\mathbf{L}^{-1}$ based on the reciprocal property of Green's function (Virieux and Operto, 2009). Following equation 12, the gradient can be efficiently constructed by applying a zero-lag crosscorrelation between the forward-modeled wavefield and back-propagated data residuals wavefield using the adjoint-state technique (Tromp et al., 2005; Plessix, 2006; Virieux and Operto, 2009). Gradient is contaminated by spurious correlations because of band-limited seismic data. It is also poorly scaled because of geometric spreading effects and uneven subsurface illumination. Hessian operator is the second-order partial derivative of the misfit function with respect to the model parameter:

$$\begin{aligned}\mathbf{H}(\mathbf{x},\mathbf{x}') &= \nabla_{\mathbf{m}(\mathbf{x})}\nabla_{\mathbf{m}(\mathbf{x}')}\Phi(\mathbf{m})\\ &= \sum_{\mathbf{x}_g}\sum_{\mathbf{x}_s}\sum_{\omega}\Re\Bigg(\frac{\partial\mathbf{u}^{\dagger}(\mathbf{x}_g,\mathbf{x}_s,\omega)}{\partial\mathbf{m}(\mathbf{x})}\frac{\partial\mathbf{u}^{*}(\mathbf{x}_g,\mathbf{x}_s,\omega)}{\partial\mathbf{m}(\mathbf{x}')}\\ &+\frac{\partial^2\mathbf{u}^{\dagger}(\mathbf{x}_g,\mathbf{x}_s,\omega)}{\partial\mathbf{m}(\mathbf{x})\partial\mathbf{m}(\mathbf{x}')}\Delta\mathbf{d}^{*}(\mathbf{x}_g,\mathbf{x}_s,\omega)\Bigg),\end{aligned} \tag{13}$$

where $\mathbf{x}'$ is the neighboring position around the position $\mathbf{x}$ (Valenciano, 2008) and $\mathbf{H}(\mathbf{x},\mathbf{x}')$ indicates one element in Hessian $\mathbf{H}$ corresponding to two model perturbations at $\mathbf{x}$ and $\mathbf{x}'$. The first term in equation 13 represents the correlation of two Fréchet derivative wavefields, and it accounts for the first-order scattering effects. Neglecting the second term in equation 13 leads to the approximate Hessian used in GN method. The two partial derivative wavefields are often to a great degree uncorrelated due to finite-frequency effects, which means that the approximate Hessian is diagonally dominant and banded (Pratt et al., 1998; Valenciano, 2008; Tang, 2009; Pan et al., 2014b, 2014c). Because of this characteristic of the approximate Hessian, GN methods can remove finite-frequency effects and deblur the gradient (Pratt et al., 1998). Furthermore, the gradient is contaminated by the second-order scattering artifacts that occur when crosscorrelating Fréchet derivative wavefield with the second-order scattered energy in the data residuals. The second term in equation 13 is the correlation of the second-order partial derivative wavefield with the data residuals. This second-order term predicts the artifacts caused by the doubly scattered energy in data residuals. Preconditioning the gradient with the full Hessian $\mathbf{H}$ is known as the FN method.

DETERMINATION OF ANISOTROPIC ELASTIC CONSTANTS WITH MULTIPARAMETER FWI

Parameter crosstalk and scattering patterns

To be separately constrained by seismic observations, the perturbation of each medium parameter type cause a unique variation in its Fréchet derivative wavefields over the observed range of scattering and azimuthal angles. Identical or nearly identical variations are one of the key mechanisms of parameter crosstalk in multiparameter FWI (Operto et al., 2013). Interaction of the incident wavefield with the model perturbation serves as the "virtual source" or "secondary scattered source." The scattering, or radiation, pattern of the "virtual source" governs the amplitude variation of Fréchet derivative wavefield as a function of scattering and azimuthal angle. An inversion sensitivity analysis taking these patterns into account is important (Gholami et al., 2013a). Coupling effects between different elastic constants are examined. Proper parameterization and optimal acquisition geometry should be calculated (Tarantola, 1986; Gholami et al., 2013b). Forgues and Lambaré (1997) study different parameter classes in acoustic and elastic ray + Born inversion. In this paper, we derive the 3D scattering patterns for elastic constants in general anisotropic media (see Appendix A).

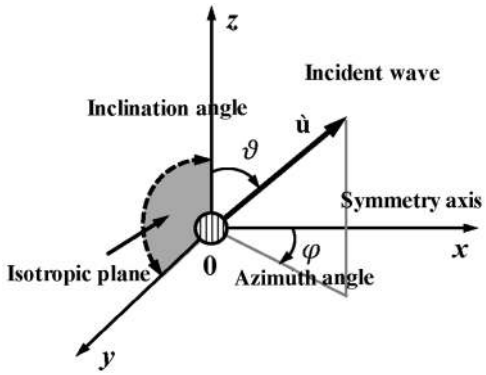

Figure 1. The 3D geometry. The function $\hat{\mathbf{u}}$ indicates normal to the wavefront of the incident wave; ϑ and φ are the inclination angle departing from z-axis and azimuth angle departing from x-axis for describing the incident wave. The HTI inclusion is at the original point 0. The x-axis is parallel to the symmetry axis of the HTI inclusion, and the y-z plane is perpendicular to the axis of symmetry.

The 3D geometry for describing the scattering problem due to the local anisotropic inclusion is presented in Figure 1. We define inclination angle ϑ and azimuth angle φ for describing the incident wave and inclination angle θ and azimuth angle ϕ for describing the scattered wave. For HTI inclusion, we also define the symmetry axis to parallel to the x-axis and the isotropic plane to be consistent with the y-z plane. The scattered wavefield due to model perturbation in general anisotropic medium is first given in equation A-10. In this research, we neglect the contribution from density and only consider the perturbation of elastic constant matrix $\delta\check{\mathbf{c}}$ for HTI media. The interaction of the incident wave with the perturbations of the elastic constants serves as the equivalent source for the scattered wavefield. The equivalent moment tensor source for the specific HTI media $\delta\check{\mathbf{M}}$ is expressed as (Ben-Menahem and Singh, 1981; Chapman, 2004)

$$\delta\check{\mathbf{M}}=\begin{bmatrix}\delta c_{11}\tilde{e}_{11}+\delta c_{13}\tilde{e}_{22}+\delta c_{13}\tilde{e}_{33} & 2\delta c_{55}\tilde{e}_{12} & 2\delta c_{55}\tilde{e}_{13}\\ 2\delta c_{55}\tilde{e}_{12} & \delta c_{13}\tilde{e}_{11}+\delta c_{33}\tilde{e}_{22}+\delta\nu\tilde{e}_{33} & 2\delta c_{44}\tilde{e}_{23}\\ 2\delta c_{55}\tilde{e}_{13} & 2\delta c_{44}\tilde{e}_{23} & \delta c_{13}\tilde{e}_{11}+\delta\nu\tilde{e}_{22}+\delta c_{33}\tilde{e}_{33}\end{bmatrix}, \tag{14}$$

where the symbol $\check{}$ represents the specification for HTI media and $\tilde{e}_{ij}$ indicate the strain components of the incident wave. Considering an incident plane P-wave (equation A-12), inserting the reduced equivalent moment tensor source $\delta\mathbb{M}$ (see equation A-18) for HTI media into equation A-19 yields the 3D scattering patterns of the elastic constants,

$$\mathbb{R}_p(\vartheta,\varphi,\theta,\phi)=\hat{\mathbf{g}}^{\dagger}\frac{\partial\mathbb{M}}{\partial\mathbf{m}}\hat{\mathbf{r}}, \tag{15}$$

where vectors $\hat{\mathbf{g}}$ and $\hat{\mathbf{r}}$ are defined in equation A-17. Perturbing one elastic constant and leaving all others unchanged, we can obtain the scattering pattern for the specified elastic constant. For example, considering the perturbation of elastic constant δc_{55}, the P-P, P-SV, and P-SH scattering coefficients due to δc_{55} can be obtained as

$$\begin{aligned}\mathbb{R}_{\mathrm{P-P}}(\vartheta,\varphi,\theta,\phi,\delta c_{55})&=4\hat{p}_1\hat{q}_2\hat{r}_1\hat{r}_2+4\hat{p}_1\hat{q}_3\hat{r}_1\hat{r}_3\\&=\sin^2\vartheta\sin 2\varphi\sin^2\theta\sin 2\phi\\&\quad+\sin 2\vartheta\cos\varphi\sin 2\theta\cos\phi.\end{aligned} \tag{16}$$

$$\begin{aligned}\mathbb{R}_{\mathrm{P-SV}}(\vartheta,\varphi,\theta,\phi,\delta c_{55})&=2\hat{p}_1\hat{q}_2\hat{\theta}_2\hat{r}_1+2\hat{p}_1\hat{q}_3\hat{\theta}_3\hat{r}_1\\&\quad+2\hat{p}_1\hat{q}_2\hat{\theta}_1\hat{r}_2+2\hat{p}_1\hat{q}_3\hat{\theta}_1\hat{r}_3\\&=\sin^2\vartheta\sin 2\varphi\sin\theta\cos\theta\sin 2\phi\\&\quad+\sin 2\vartheta\cos\varphi\cos 2\theta\cos\phi.\end{aligned} \tag{17}$$

$$\begin{aligned}\mathbb{R}_{\mathrm{P-SH}}(\vartheta,\varphi,\theta,\phi,\delta c_{55})&=2\hat{p}_1\hat{q}_2\hat{\phi}_2\hat{r}_1+2\hat{p}_1\hat{q}_3\hat{\phi}_3\hat{r}_1\\&\quad+2\hat{p}_1\hat{q}_2\hat{\phi}_1\hat{r}_2+2\hat{p}_1\hat{q}_3\hat{\phi}_1\hat{r}_3\\&=\sin^2\vartheta\sin 2\varphi\sin\theta\cos 2\phi\\&\quad-\sin 2\vartheta\cos\varphi\sin\phi\cos\theta.\end{aligned} \tag{18}$$

Figure 2a–2c shows the 3D P-P (equation 16), P-SV (equation 17), and P-SH (equation 18) scattering patterns due to δc_{55} ($\vartheta = 135^{o}$ and $\varphi = 0^{o}$). Figure 3a–3c shows the P-P scattering patterns due to perturbations of c_{33}, c_{11}, and c_{13} respectively. The scattered P-wave, SV-wave, and SH-wave with incident plane SV-wave and incident plane SH-wave can be obtained following equations A-24 and A-25. If the scattering patterns associated with different elastic constants significantly overlap a range of scattering angle or azimuth angle, the parameter crosstalk between these physical parameters will contaminate the update. If the update is not properly preconditioned, the inversion process will be impacted negatively. This difficulty also raises the parameterization issue for managing parameter crosstalk. Determining a more proper parameterization for inverting fracture properties using FWI is beyond the scope of this research. The 3D scattering patterns of the elastic constants in general anisotropic media given in this paper can be transformed to the scattering patterns for any parameter class using the chain rule.

Multiparameter Hessian

The role of the single-parameter Hessian has been discussed and analyzed in the previous section. The multiparameter Hessian in multiparameter FWI has a block structure, and it carries more information than the single-parameter Hessian. Considering a 2D subsurface model with $N_x N_z$ nodes and N_p physical parameters are assigned to describe the properties of each node, where N_x and N_z denote the numbers of grid nodes in horizontal and vertical directions, respectively. The multiparameter Hessian is a $N_x N_z N_p \times N_x N_z N_p$ square and symmetric matrix with N_p diagonal blocks and $N_p(N_p-1)$ off-diagonal blocks. Each block is a $N_x N_z \times N_x N_z$ square matrix. Hence, the multiparameter Hessian $\mathbf{H}$ for inversing the four elastic constants in 2D HTI media has 16 block submatrices ($N_p = 4$),

$$\mathbf{H} = \begin{bmatrix} \mathbf{H}_{3333} & \mathbf{H}_{3355} & \mathbf{H}_{3311} & \mathbf{H}_{3313} \\ \mathbf{H}_{5533} & \mathbf{H}_{5555} & \mathbf{H}_{5511} & \mathbf{H}_{5513} \\ \mathbf{H}_{1133} & \mathbf{H}_{1155} & \mathbf{H}_{1111} & \mathbf{H}_{1113} \\ \mathbf{H}_{1333} & \mathbf{H}_{1355} & \mathbf{H}_{1311} & \mathbf{H}_{1313} \end{bmatrix}, \tag{19}$$

where the subscripts of the block matrices in $\mathbf{H}$ are consistent with the subscripts of two elastic constants. The multiparameter Hessian $\mathbf{H}$ can be written as the summation of the first-order term $\tilde{\mathbf{H}}$ and the second-order term $\bar{\mathbf{H}}$. The element $\tilde{\mathbf{H}}_{\mathbf{m}_1\mathbf{m}_2}(\mathbf{x},\mathbf{x}')$ within multiparameter GN Hessian $\tilde{\mathbf{H}}$ indicates the correlation of Fréchet derivative wavefields with respect to model parameters $\mathbf{m}_1$ and $\mathbf{m}_2$:

$$\tilde{\mathbf{H}}_{\mathbf{m}_1\mathbf{m}_2}(\mathbf{x},\mathbf{x}') = \sum_{\mathbf{x}_s}\sum_{\mathbf{x}_g}\sum_{\omega} \Re\left(\frac{\partial \mathbf{u}^{\dagger}(\mathbf{x}_g,\mathbf{x}_s,\omega)}{\partial \mathbf{m}_1(\mathbf{x})}\frac{\partial \mathbf{u}^{*}(\mathbf{x}_g,\mathbf{x}_s,\omega)}{\partial \mathbf{m}_2(\mathbf{x}')}\right), \tag{20}$$

where when $\mathbf{m}_1 = \mathbf{m}_2$, it indicates the element in diagonal block, and when $\mathbf{m}_1 \neq \mathbf{m}_2$, it indicates the element in an off-diagonal

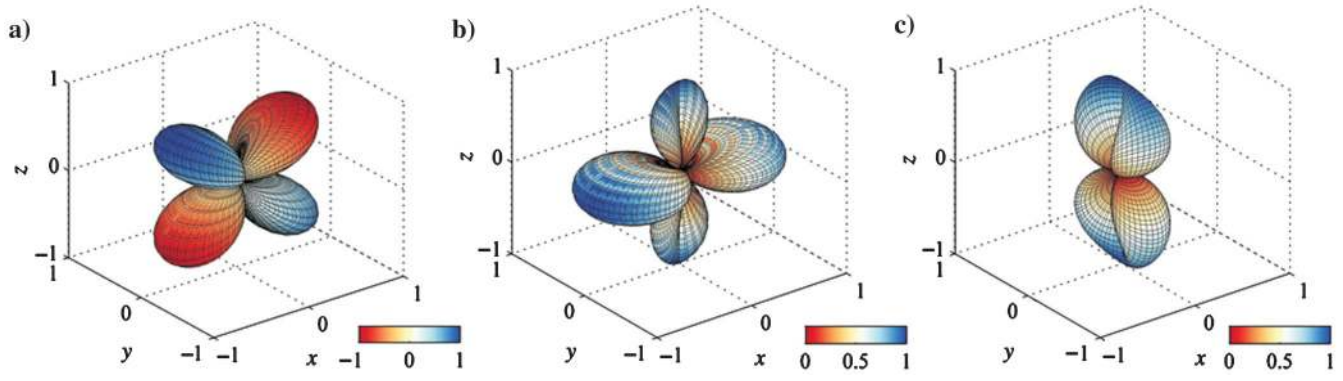

Figure 2. Panels (a-c) show the P-P (equation 16), P-SV (equation 17), and P-SH (equation 18) scattering patterns due to the perturbation of c_{55}.

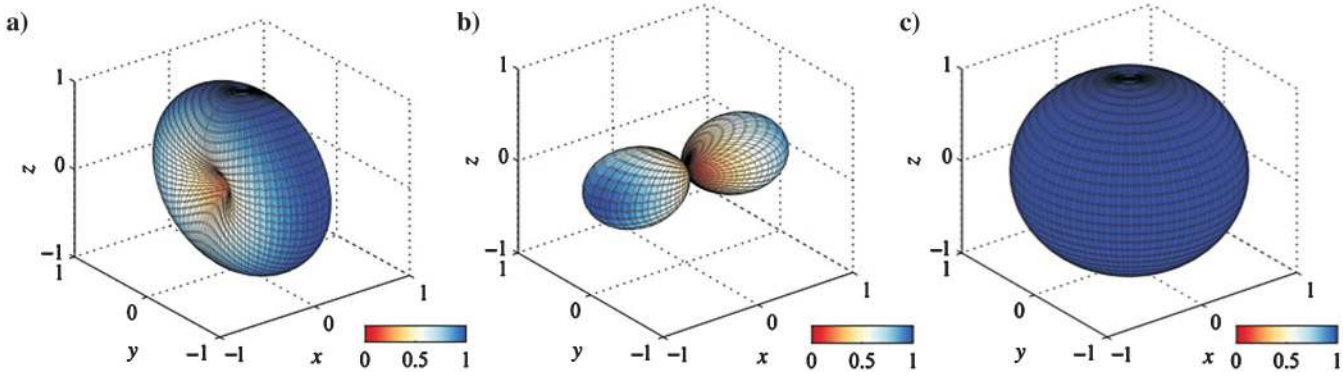

Figure 3. Panels (a-c) show the P-P scattering patterns due to the perturbations of c_{33}, c_{13}, and c_{11}, respectively.

block. The multiparameter approximate Hessian $\tilde{\mathbf{H}}$ is essential in overcoming the crosstalk difficulty in multiparameter FWI (Operto et al., 2013; Pan et al., 2015b). As we discussed in the previous section, the similarity of the Fréchet derivative wavefields with respect to different physical parameters gives rise to the crosstalk problem. The off-diagonal blocks in multiparameter approximate Hessian, as indicated by the gray boxes in Figure 4, predict the coupling effects and applying its inverse to the gradient can remove or mitigate the parameter crosstalk.

The space-type multiparameter Hessian approximation $\tilde{\mathbf{H}}_\mathbf{s}$ given by Innanen (2014a) neglects the contributions of the off-diagonal blocks and stresses the correlation of Fréchet derivative wavefields with respect to the same physical parameter, as indicated by the four black diagonal boxes in Figure 4. This approximation can scale the amplitudes of the gradient and deblur the gradient, but cannot suppress parameter crosstalk. The parameter-type multiparameter Hessian approximation $\tilde{\mathbf{H}}_\mathbf{p}$ (as indicated by the white dashed lines in Figure 4) only keeps the diagonal elements of the blocks, which is also capable of mitigating parameter crosstalk but limited in resolving the gradient.

Similarly, when correlating the Fréchet derivative wavefields with the data residuals in multiparameter FWI, the doubly scattered energy in the data residuals will result in artifacts or spurious correlations in the gradient. The second-order term $\tilde{\mathbf{H}}$ in multiparameter Hessian associated with second-order scattering effects works as a demultiple operator to suppress these artifacts. The second-order partial derivative wavefields for multiparameter Hessian become more complex. Figure 5 shows a schematic diagram for multiparameter second-order scattering effects. Fréchet derivative wavefield $\partial\mathbf{u}(\mathbf{x}_g,\mathbf{x}_s,\omega)/\partial\mathbf{m}_1(\mathbf{x})$ due to the perturbation of model parameter $\mathbf{m}_1(\mathbf{x})$, is scattered secondly due to the perturbation of physical parameter $\mathbf{m}_2(\mathbf{x}')$, which yields the second-order partial derivative wavefields $\partial^2\mathbf{u}(\mathbf{x}_g,\mathbf{x}_s,\omega)/\partial\mathbf{m}_1(\mathbf{x})\partial\mathbf{m}_2(\mathbf{x}')$. Hence, the gradient will be contaminated by artifacts due to the multiparameter doubly scattered energy. These artifacts can be suppressed by the second-order term in multiparameter Hessian. Although it is quite expensive to calculate this second-order preconditioner explicitly, we will show that it can be constructed using the adjoint-state method more efficiently.

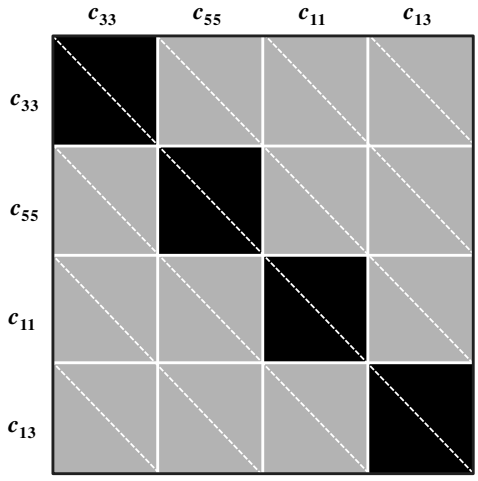

Figure 4. The schematic diagram of the multiparameter approximate Hessian $\tilde{\mathbf{H}}$ associated with the elastic constants c_{33}, c_{55}, c_{11}, and c_{13}.

Constructing multiparameter second-order preconditioner with the adjoint-state method

To calculate the second-order preconditioner for single-parameter FWI explicitly, $(N_xN_z)^2/2$ forward modeling problems need to be solved, which is extremely expensive (Pratt et al., 1998). Considering the first-order partial derivative wavefield in equation 11, we can take partial derivative with respect to model parameter $\mathbf{m}(\mathbf{x}')$ on both sides of equation 11, which gives the equation describing the propagation of the second-order partial derivative wavefield:

$$\mathbf{L}(\mathbf{m},\omega)\frac{\partial^2\mathbf{u}(\mathbf{x}_g,\mathbf{x}_s,\omega)}{\partial\mathbf{m}(\mathbf{x})\partial\mathbf{m}(\mathbf{x}')}=\tilde{\tilde{\mathbf{f}}}_s(\mathbf{x},\mathbf{x}',\omega), \tag{21}$$

where $\tilde{\tilde{\mathbf{f}}}_s(\mathbf{x},\mathbf{x}',\omega)$ indicates the second-order virtual source:

$$\tilde{\tilde{\mathbf{f}}}_s(\mathbf{x},\mathbf{x}',\omega)=-\frac{\partial\mathbf{L}(\mathbf{m},\omega)}{\partial\mathbf{m}(\mathbf{x})}\frac{\partial\mathbf{u}(\mathbf{x}_g,\mathbf{x}_s,\omega)}{\partial\mathbf{m}(\mathbf{x}')}-\frac{\partial\mathbf{L}(\mathbf{m},\omega)}{\partial\mathbf{m}(\mathbf{x}')}\frac{\partial\mathbf{u}(\mathbf{x}_g,\mathbf{x}_s,\omega)}{\partial\mathbf{m}(\mathbf{x})}$$
$$-\frac{\partial^2\mathbf{L}(\mathbf{m},\omega)}{\partial\mathbf{m}(\mathbf{x})\partial\mathbf{m}(\mathbf{x}')}\mathbf{u}(\mathbf{x}_g,\mathbf{x}_s,\omega), \tag{22}$$

where the first term indicates the second-order virtual source constructed by the interaction of Fréchet derivative wavefield $\partial\mathbf{u}(\mathbf{x}_g,\mathbf{x}_s,\omega)/\partial\mathbf{m}(\mathbf{x}')$ with model perturbation $\delta\mathbf{m}(\mathbf{x})$. Its second term is the interaction of Fréchet derivative wavefield $\partial\mathbf{u}(\mathbf{x}_g,\mathbf{x}_s,\omega)/\partial\mathbf{m}(\mathbf{x})$ with model perturbation $\delta\mathbf{m}(\mathbf{x}')$. In single-parameter FWI, the third term in equation 22 is zero when $\mathbf{x}\neq\mathbf{x}'$. Isolating the second-order partial derivative wavefield in equation 21 and inserting it into the second term of equation 13 yields

$$\bar{\mathbf{H}}(\mathbf{x},\mathbf{x}')=\sum_{\mathbf{x}_g}\sum_{\mathbf{x}_s}\sum_{\omega}\Re(\tilde{\tilde{\mathbf{f}}}_s^{\dagger}(\mathbf{x},\mathbf{x}',\omega)\mathbf{L}^{-1}(\mathbf{m},\omega)\Delta\mathbf{d}^*(\mathbf{x}_g,\mathbf{x}_s,\omega)). \tag{23}$$

It can be observed that equation 23 is similar to equation 12 for gradient calculation using the adjoint-state technique. The term $\mathbf{L}^{-1}(\mathbf{m},\omega)\Delta\mathbf{d}^*(\mathbf{x}_g,\mathbf{x}_s,\omega)$ serves as the back-propagated residual wavefield. Thus, the second-order preconditioner can be constructed by multiplying the back-propagated wavefield with the second-order

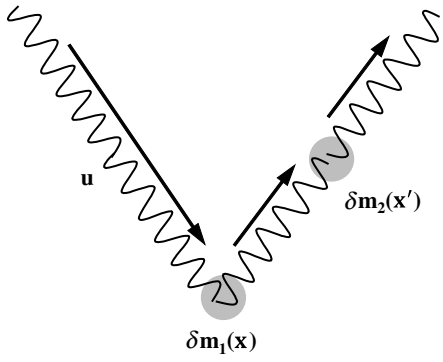

Figure 5. Schematic diagram of multiparameter second-order scattering. The indicate wavefields $\mathbf{u}$ is first scattered by the model perturbation $\delta\mathbf{m}_1$ at $\mathbf{x}$ and then scattered again by model perturbation $\delta\mathbf{m}_2$ at $\mathbf{x}'$.

virtual source using the adjoint-state method, which only needs $N_x N_z$ additional forward modeling problems (Pratt et al., 1998).

It is more complex to construct the second-order preconditioner in multiparameter Hessian because the second-order partial derivative wavefield can be caused by perturbations of different physical parameters. Considering two different physical parameters $\mathbf{m}_1$ and $\mathbf{m}_2$ and following equation 21, we can obtain the wave equation describing the propagation of multiparameter second-order scattered wavefield:

$$\mathbf{L}(\mathbf{m},\omega)\frac{\partial^2\mathbf{u}(\mathbf{x}_g,\mathbf{x}_s,\omega)}{\partial\mathbf{m}_1(\mathbf{x})\partial\mathbf{m}_2(\mathbf{x}')}=\tilde{\tilde{\mathbf{f}}}_{\mathbf{m}_1\mathbf{m}_2}(\mathbf{x},\mathbf{x}',\omega). \tag{24}$$

To construct the second-order partial derivative wavefield explicitly, $(N_p N_x N_z)^2/2$ forward modeling problems need to be solved. The function $\tilde{\tilde{\mathbf{f}}}_{\mathbf{m}_1\mathbf{m}_2}(\mathbf{x},\mathbf{x}',\omega)$ in equation 24 is the multiparameter second-order virtual source:

$$\begin{aligned}\tilde{\tilde{\mathbf{f}}}_{\mathbf{m}_1\mathbf{m}_2}(\mathbf{x},\mathbf{x}',\omega)=&-\frac{\partial\mathbf{L}(\tilde{\mathbf{m}},\omega)}{\partial\mathbf{m}_1(\mathbf{x})}\frac{\partial\mathbf{u}(\mathbf{x}_g,\mathbf{x}_s,\omega)}{\partial\mathbf{m}_2(\mathbf{x}')}\\&-\frac{\partial\mathbf{L}(\tilde{\mathbf{m}},\omega)}{\partial\mathbf{m}_1(\mathbf{x}')}\frac{\partial\mathbf{u}(\mathbf{x}_g,\mathbf{x}_s,\omega)}{\partial\mathbf{m}_2(\mathbf{x})}-\frac{\partial^2\mathbf{L}(\tilde{\mathbf{m}},\omega)}{\partial\mathbf{m}_1(\mathbf{x})\partial\mathbf{m}_2(\mathbf{x}')}\mathbf{u}(\mathbf{x}_g,\mathbf{x}_s,\omega),\end{aligned} \tag{25}$$

where $\tilde{\mathbf{m}}$ denotes all of the physical parameters considered. The first term in equation 25 indicates the multiparameter second-order virtual source caused by the interaction of the Fréchet derivative wavefield $\partial\mathbf{u}(\mathbf{x}_g,\mathbf{x}_s,\omega)/\partial\mathbf{m}_1(\mathbf{x}')$ with $\delta\mathbf{m}_2(\mathbf{x})$. The second term is formed by the interaction of the Fréchet derivative wavefield $\partial\mathbf{u}(\mathbf{x}_g,\mathbf{x}_s,\omega)/\partial\mathbf{m}_2(\mathbf{x})$ with $\delta\mathbf{m}_1(\mathbf{x}')$. The value of the third term in equation 25 is determined by the parameterization for describing the subsurface media. If $\mathbf{m}_1$ and $\mathbf{m}_2$ are independent physical parameters, the third term in equation 25 is zero. However, if $\mathbf{m}_1$ and $\mathbf{m}_2$ are not independent physical parameters (e.g., P-wave velocity α and density ρ), the third term is not zero (Fichtner and Trampert, 2011). In this research, this term is ignored because the four elastic constants used to describe the 2D HTI media are independent.

It is also possible for us to calculate the second-order preconditioner for multiparameter FWI using the adjoint-state technique. Similar to equation 23, the multiparameter second-order preconditioner can be expressed as

$$\begin{aligned}\tilde{\mathbf{H}}_{\mathbf{m}_1\mathbf{m}_2}(\mathbf{x},\mathbf{x}')=&\sum_{\mathbf{x}_g}\sum_{\mathbf{x}_s}\sum_{\omega}\Re(\tilde{\tilde{\mathbf{f}}}^{\dagger}_{\mathbf{m}_1\mathbf{m}_2}(\mathbf{x},\mathbf{x}',\omega)\\&\times\mathbf{L}^{-1}(\tilde{\mathbf{m}},\omega)\Delta\mathbf{d}^{*}(\mathbf{x}_g,\mathbf{x}_s,\omega)).\end{aligned} \tag{26}$$

Thus, additional $N_p N_x N_z$ forward modeling simulations are required for constructing the multiparameter second-order preconditioner. For example, to inverse the four elastic constants in HTI media, the off-diagonal block $\tilde{\mathbf{H}}_{c_{33}c_{55}}$ in the second-order preconditioner is expressible as

$$\begin{aligned}\tilde{\mathbf{H}}_{c_{33}c_{55}}(\mathbf{x},\mathbf{x}')=&\sum_{\mathbf{x}_g}\sum_{\mathbf{x}_s}\sum_{\omega}\Re(\tilde{\tilde{\mathbf{f}}}^{\dagger}_{c_{33}c_{55}}(\mathbf{x},\mathbf{x}',\omega)\\&\mathbf{L}^{-1}(\tilde{\mathbf{m}},\omega)\Delta\mathbf{d}^{*}(\mathbf{x}_g,\mathbf{x}_s,\omega)),\end{aligned} \tag{27}$$

where $\tilde{\mathbf{m}}$ indicates all of the four elastic constants c_{33}, c_{55}, c_{11}, and c_{13}.

NUMERICAL EXAMPLES

In this section, we provide several numerical examples for testing the proposed strategies. We first examine the scattering patterns of the elastic constants in HTI media by comparing analytic results with numerical results and explain the parameter crosstalk problem. We then introduce the multiparameter Hessian using a 2D HTI model and illustrate its effectiveness in suppressing parameter crosstalk and second-order scattering effects. Finally, we enact the GN and FN multiparameter FWI on a two-block-layer model.

Scattering patterns of the elastic constants: Analytic versus numerical results

In this numerical example, we examine the analytic and numerical scattering patterns of the elastic constants for parameter crosstalk analysis. The x-z plane with zero azimuth angle in 3D geometry (Figure 1) is extracted, which forms the specified 2D HTI model. The acquisition geometry is shown in Figure 6. The model consists of 320×320 grid cells with grid sizes $\Delta x=\Delta z=5$ m. The background model is isotropic and elastic with elastic constants $c_{33}=14.06$, $c_{55}=6.32$, $c_{11}=14.06$, and $c_{13}=1.42$ GPa (P-wave velocity $\alpha=2651.4$ m/s, S-wave velocity $\beta=1777.6$ m/s, density $\rho=2.0$ g/cm^3). In total, -10% perturbations are applied to the elastic constants of the node located at the center of the model, which forms the anisotropic anomaly (the black circle point in Figure 6). One source is located at top-left corner of the 2D model, as indicated by the black star in Figure 6. When the incident P-wave ($\vartheta=135^{\circ}$ and $\varphi=0^{\circ}$) interacts with the HTI anomaly, the scattered wave will propagate at all directions and its amplitudes change with varying angle θ. The receivers are deployed along the top surface of the model for a reflection survey, which means that we can only record the scattered wave at the range of $\theta\in[315^{\circ},360^{\circ}]$ and $\theta\in[0^{\circ},45^{\circ}]$.

We extract the x-z plane from the analytic 3D scattering patterns for these elastic constants. The bold-black curves in Figure 7a–7d show the P-P scattering patterns due to δc_{33}, δc_{55}, δc_{11}, and δc_{13} with incident P-wave ($\vartheta=135^{\circ}$ and $\varphi=0^{\circ}$). Perturbations of different elastic constants serve as different types of secondary sources associated with different scattering patterns. The P-SV scattering pattern due to δc_{33} is also plotted as indicated by the blue curve in Figure 7a. The analytic scattering patterns are overlain by numerical modeling results for comparison. The amplitude variations of the analytic scattering patterns are consistent with those of the numerical results.

In angle regimes where the scattering pattern of one parameter is indistinguishable from that of another, the influences of the two parameters are not separable, and crosstalk appears. Comparing the scattering pattern in Figure 7a with that in Figure 7d, for instance, we observe that the P-P scattering patterns due to δc_{33} and δc_{13} are significantly overlapped at near offset, indicating strong crosstalk between c_{33} and c_{13} for this reflection survey. Furthermore, parameter crosstalk between c_{55} and c_{13} is very strong at mid-offset. In Figure 7c, we also observe that strong scattered wavefields response due to δc_{11} can only be recorded at large offset. For inversing the elastic constants using FWI, the parameter crosstalk among these parameters are strong and complex for this reflection acquis-

ition survey, which will undermine the inversion process without proper preconditioning.

Suppressing crosstalk with multiparameter approximate Hessian

To examine the ability of the multiparameter approximate Hessian to suppress parameter crosstalk, we enact a GN update on a 2D HTI point scatterer model. The 2D HTI model consists of 900 nodes ($N_x = N_z = 30$) with grid size of 5 m in the horizontal and vertical dimensions and four elastic constants (c_{33}, c_{55}, c_{11}, and c_{13}) are used to describe each node. The initial model is elastic and isotropic with elastic constants $c_{33} = 14.06$, $c_{55} = 6.32$, $c_{11} = 14.06$, and $c_{13} = 1.42$ GPa. The true model is built by embedding one HTI point anomaly at the center position of the background model. Four elastic constants are all perturbed by -10% at this point scatterer. A 50 Hz Ricker wavelet is used for forward modeling, and the absorbing boundary condition is applied on all of the boundaries of the model. In these numerical examples presented in this research, multicomponent data are used for inversion.

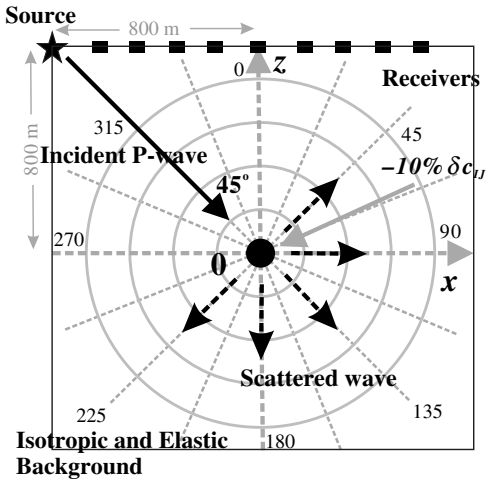

Figure 6. The 2D numerical model for examining the scattering patterns of elastic constants. The black point at the center of the model indicates the HTI anomaly at position $\mathbf{x}_0$ = (0 m, 0 m, 0 m). The source is located at $\mathbf{x}_s$ = (−800 m, 0 m, 800 m). The receivers (the black squares) are arranged along the top surface for a reflection survey.

First, the multiparameter approximate Hessian $\tilde{\mathbf{H}}$ is constructed explicitly with one source located at $\mathbf{x}_{s1}$ = (75 m, 0 m, 0 m). Thirty receivers are arranged along the top surface of the model with a spacing of 5 m. As shown in Figure 8, the multiparameter approximate Hessian is a 3600×3600 square and symmetric matrix with four diagonal blocks and 12 off-diagonal blocks, which are consistent with the schematic diagram shown in Figure 4. Each block matrix is a 900×900 square matrix.

It can be seen that the subblocks in multiparameter approximate Hessian are banded due to finite-frequency effects. Because elastic constant c_{33} directly relates to P-wave velocity α ($c_{33} = \rho\alpha^2$) and the Fréchet derivative wavefield caused by δc_{33} recorded at the receivers are much stronger than those due to other elastic constants, the diagonal block $\tilde{\mathbf{H}}_{3333}$ dominates the whole matrix. The four diagonal blocks $\tilde{\mathbf{H}}_{3333}$, $\tilde{\mathbf{H}}_{5555}$, $\tilde{\mathbf{H}}_{1111}$, and $\tilde{\mathbf{H}}_{1313}$ are extracted, as shown in Figure 9a–9d, respectively (the amplitudes have been renormalized). These four diagonal blocks form the space-type multi-

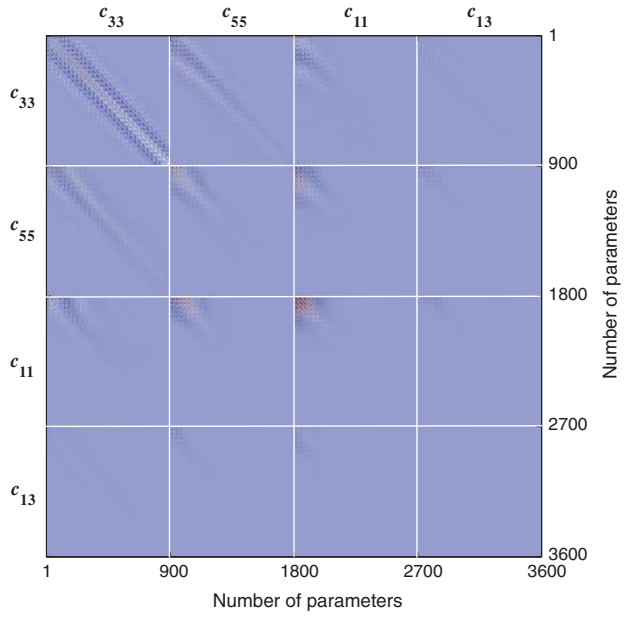

Figure 8. The multiparameter approximate Hessian $\tilde{\mathbf{H}}$ for elastic constants c_{33}, c_{55}, c_{11}, and c_{13} with the 2D HTI model. The multiparameter approximate Hessian is a 3600×3600 square and symmetric matrix ($N_p = 4$ and $N_x = N_z = 30$).

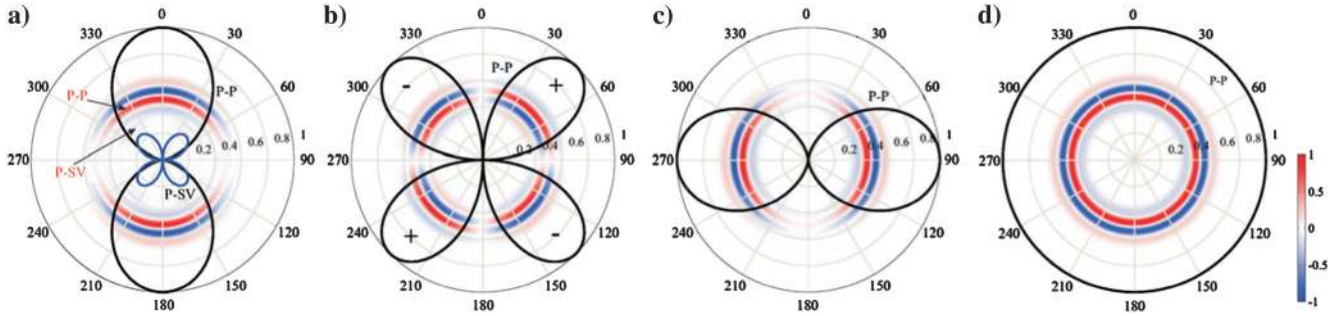

Figure 7. Analytic versus numerical results of the scattering patterns for the elastic constants in 2D HTI media. Panels (a-d) show the scattering patterns due to elastic constants δc_{33}, δc_{55}, δc_{11}, and δc_{13}, respectively. The symbols "+" and "−" in (b) mean positive and negative polarities of the scattered wave. The amplitudes have been normalized.

parameter Hessian approximation $\tilde{\mathbf{H}}_s$ given by Innanen (2014b). Furthermore, we can see that the energy distributions in the four diagonal blocks are quite different, which are determined by the scattering patterns of these elastic constants.

The diagonal elements in the diagonal blocks $\tilde{\mathbf{H}}_{3333}$, $\tilde{\mathbf{H}}_{5555}$, $\tilde{\mathbf{H}}_{1111}$, and $\tilde{\mathbf{H}}_{1313}$ are extracted and plotted in model space (as shown in Figure 10a–10d), and they mainly account for illumination compensation and removing the geometric spreading effects. The parameter crosstalk between different physical parameters are measured by the 12 off-diagonal blocks of $\tilde{\mathbf{H}}$, as shown in Figure 8. Stronger amplitudes in the off-diagonal blocks means stronger parameter crosstalk. Figure 10e–10j shows the diagonal elements of the off-diagonal blocks $\tilde{\mathbf{H}}_{3355}$, $\tilde{\mathbf{H}}_{3311}$, $\tilde{\mathbf{H}}_{3313}$, $\tilde{\mathbf{H}}_{5511}$, $\tilde{\mathbf{H}}_{5513}$, and $\tilde{\mathbf{H}}_{1113}$, respectively, which mainly account for removing the parameter crosstalk (Innanen, 2014b).

We now present a numerical example to show that preconditioning the gradient with the multiparameter approximate Hessian $\tilde{\mathbf{H}}$ can suppress parameter crosstalk and resolve the gradient. The search direction $\Delta\mathbf{m}_n$ associated with the GN update can be obtained by solving the Newton linear system (equation 6) approximately using a conjugate-gradient (CG) algorithm, which is known as the truncated-Newton method (Fichtner and Trampert, 2011; Métivier et al., 2013). In this paper, the gradient is preconditioned by the pseudo-inverse of the multiparameter approximate Hessian $\tilde{\mathbf{H}}^{-1}$, which is calculated using singular value decomposition (SVD).

First, the data residual vector $\Delta\mathbf{d}_{33}$ caused by perturbation of c_{33} is used to construct the gradients of all elastic constants c_{33}, c_{55}, c_{11}, and c_{13}. Figure 11a–11d shows the gradient vectors $\nabla_{c_{33}}\Phi$, $\nabla_{c_{55}}\Phi$, $\nabla_{c_{11}}\Phi$, and $\nabla_{c_{13}}\Phi$ without multiparameter approximate Hessian preconditioning, respectively. Only the gradient vector $\nabla_{c_{33}}\Phi$ is real and the gradient vectors for other elastic constants are all artifacts caused by parameter crosstalk. We then apply the multiparameter approximate Hessian $\tilde{\mathbf{H}}$ to precondition the gradient vectors and the estimated model perturbations for the elastic constants c_{33}, c_{55}, c_{11}, and c_{13} are illustrated in Figure 11e–11h, respectively. It can be observed that the artifacts in Figure 11b–11d have been obviously removed, and the estimated model perturbation for c_{33} in Figure 11a is resolved and deblurred. Figure 11i–11l shows the gradient vectors calculated using the data residual vector $\Delta\mathbf{d}_{55}$ due to δc_{55}. Similarly, only the gradient vector $\nabla_{c_{55}}\Phi$ in Figure 11j is real and other gradient vectors in Figure 11i, 11k, and 11l are all spurious correlations. Figure 11m–11p shows the model perturbation estimations with multiparameter approximate Hessian preconditioning for the four elastic constants, respectively. It can be seen

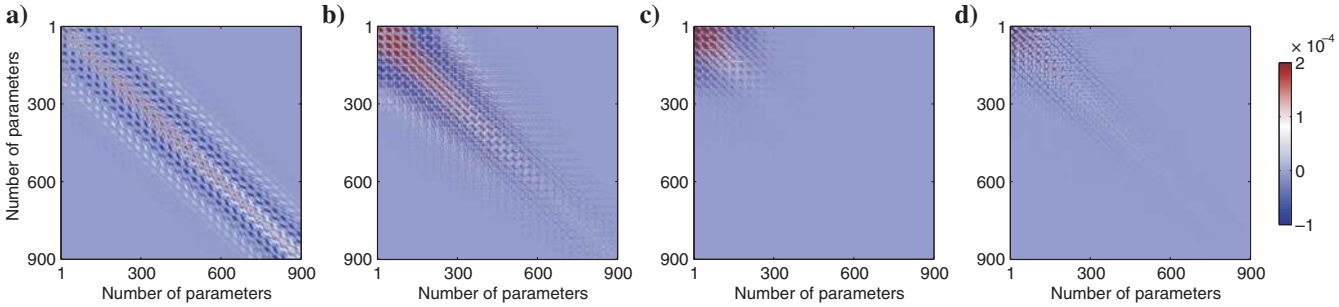

Figure 9. The diagonal blocks of the multiparameter approximate Hessian shown in Figure 8. Panels (a-d) show the diagonal blocks $\tilde{\mathbf{H}}_{3333}$, $\tilde{\mathbf{H}}_{5555}$, $\tilde{\mathbf{H}}_{1111}$, and $\tilde{\mathbf{H}}_{1313}$ of the multiparameter approximate Hessian, respectively.

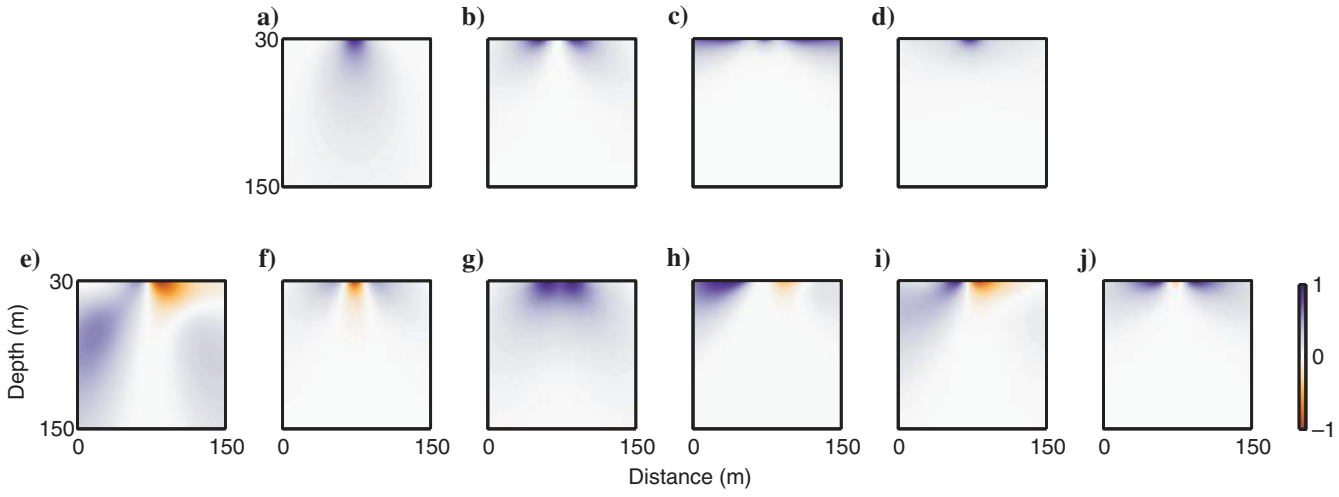

Figure 10. The diagonal elements of the block matrices plotted in model space. Panels (a-d) show the diagonal elements of the diagonal block matrices $\tilde{\mathbf{H}}_{3333}$, $\tilde{\mathbf{H}}_{5555}$, $\tilde{\mathbf{H}}_{1111}$, and $\tilde{\mathbf{H}}_{1313}$, respectively. Panels (e-j) show the diagonal elements of the off-diagonal block matrices $\tilde{\mathbf{H}}_{3355}$, $\tilde{\mathbf{H}}_{3311}$, $\tilde{\mathbf{H}}_{3313}$, $\tilde{\mathbf{H}}_{5511}$, $\tilde{\mathbf{H}}_{5513}$, and $\tilde{\mathbf{H}}_{1113}$, respectively. Because the symmetry of the multiparameter approximate Hessian $\tilde{\mathbf{H}}$, we only plot the diagonal elements of six off-diagonal blocks in $\tilde{\mathbf{H}}$.

that the artifacts in Figure 11i, 11k, and 11l are suppressed, and the gradient vector $\nabla_{c_{55}}\Phi$ in Figure 11j is resolved obviously. These two numerical examples show the ability of the multiparameter approximate Hessian in suppressing parameter crosstalk artifacts and resolving the gradient vectors.

Figure 12a–12d shows the gradient vectors obtained using the data residuals $\Delta\mathbf{d}$ due to the perturbations of four elastic constants with three sources. The three sources are located at $\mathbf{x}_{s1}$ = (75 m, 0 m, 0 m), $\mathbf{x}_{s2}$ = (0 m, 0 m, 0 m), and $\mathbf{x}_{s3}$ = (150 m, 0 m, 0 m), respectively. Figure 12e–12h shows the estimated model perturbations with multiparameter approximate Hessian preconditioning. Figure 12i–12l shows the estimated model perturbations of the elastic constants using GN multiparameter FWI after three iterations. It can be seen that the four elastic constants can be inverted simultaneously very well with multiparameter approximate Hessian preconditioning.

Suppressing multiparameter second-order scattering effects

In this numerical example, we show the effectiveness of the second-order preconditioner in suppressing multiparameter second-order scattering effects. The second-order term $\bar{\mathbf{H}}$ is constructed by correlating the second-order partial derivative wavefields with the data residuals. When considering multiple physical parameters, the second-order partial derivative wavefields can be caused by different physical parameters. Furthermore, it is quite expensive to calculate the second-order term directly. In this research, we use the adjoint-state method for calculating the second-order term $\bar{\mathbf{H}}$ in the multiparameter Hessian $\mathbf{H}$.

Considering the elastic and isotropic background model used in previous example, two HTI point anomalies are embedded in the background model as shown in Figure 13. The two HTI points anomalies are located at $\mathbf{x}_1$ = (80 m, 0 m, 65 m) and $\mathbf{x}_2$ = (90 m, 0 m, 75 m). At position $\mathbf{x}_1$, the elastic constants c_{33}, c_{55}, c_{11}, and c_{13} are perturbed by +10%, +10%, 0%, and +10%, respectively. At position $\mathbf{x}_2$, the four elastic constants are perturbed by −10%, −10%, −10%, and 0%, respectively. The normalized true model perturbations for elastic constants c_{33}, c_{55}, c_{11}, and c_{13} are illustrated in Figure 13a–13d, respectively.

Figure 14 shows the elements of the first- and second-order terms of the multiparameter Hessian plotted in model space. Considering the model parameter position $\mathbf{x}_2$, the correlation of the Fréchet derivative wavefield due to $\delta c_{33}(\mathbf{x}_2)$ with the Fréchet derivative wavefields due to $\delta c_{33}(\tilde{\mathbf{x}})$ ($\tilde{\mathbf{x}}$ indicate all positions in the model) forms the 555th row in diagonal block $\tilde{\mathbf{H}}_{3333}$, as shown in Figure 14a. Figure 14b–14d shows the 555th rows in the off-diagonal blocks $\tilde{\mathbf{H}}_{3355}$, $\tilde{\mathbf{H}}_{3311}$, and $\tilde{\mathbf{H}}_{3313}$, respectively. Stronger amplitudes mean stronger correlations of the Fréchet derivative wavefields.

The Fréchet derivative wavefield due to $\delta c_{33}(\mathbf{x}_2)$ can be further scattered due to $\delta c_{33}(\tilde{\mathbf{x}})$ or $\delta c_{55}(\tilde{\mathbf{x}})$, $\delta c_{11}(\tilde{\mathbf{x}})$, and $\delta c_{13}(\tilde{\mathbf{x}})$. Correlating the multiparameter second-order scattered wavefield with the data residuals forms the 555th rows of diagonal block $\tilde{\mathbf{H}}_{3333}$, off-diagonal blocks $\tilde{\mathbf{H}}_{3355}$, $\tilde{\mathbf{H}}_{3311}$, and $\tilde{\mathbf{H}}_{3313}$, as shown in Figure 14e–14h, which are obtained using explicit perturbation method with additional 900 forward modeling simulations (Pratt et al., 1998). Stronger amplitudes mean stronger correlations between the second-order scattered wavefields with the data residuals. Figure 14i–14l shows the 555th rows in blocks $\tilde{\mathbf{H}}_{3333}$, $\tilde{\mathbf{H}}_{3355}$, $\tilde{\mathbf{H}}_{3311}$, and $\tilde{\mathbf{H}}_{3313}$ calculated using the adjoint-state method following equation 27 with additional one forward modeling simulation. Constructing the multiparameter second-order preconditioner with the adjoint-state method, an additional 3600 forward modeling simulations are required.

We give a numerical example to show the artifacts caused by the second-order scattering effects. Figure 15a–15d shows the GN updates for δc_{33} when the true model perturbation δc_{33} was increased from 10% to 20%, 30%, and 40%, respectively. Larger model perturbation means stronger second-order scattered energy in the data residuals. It can be seen that the artifacts become stronger with increasing the model perturbation. Figure 15e–15h shows the GN updates for c_{55} when increasing the model perturbation

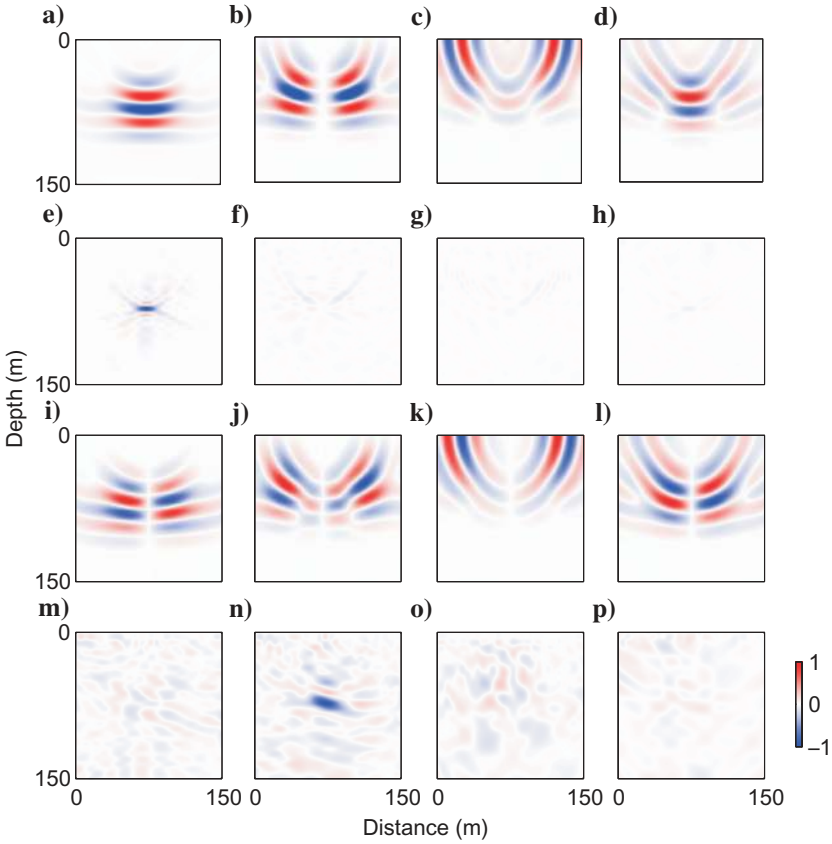

Figure 11. Panels (a-d) show the gradient vectors $\nabla_{c_{33}}\Phi$, $\nabla_{c_{55}}\Phi$, $\nabla_{c_{11}}\Phi$, and $\nabla_{c_{13}}\Phi$ constructed by the data residual vector $\Delta\mathbf{d}_{33}$. Panels (e-h) show the perturbation estimations after multiparameter approximate Hessian preconditioning for the corresponding elastic constants. Panels (i-l) show the gradient vectors constructed by data residual vector $\Delta\mathbf{d}_{55}$ for the corresponding elastic constants. Panels (m-p) show the perturbation estimations for the corresponding elastic constants with multiparameter approximate Hessian preconditioning.

δc_{33}. We can see that the artifacts become very strong in Figure 15g and 15h. It is difficult to recognize the anomalies at positions $\mathbf{x}_1$ and $\mathbf{x}_2$. This means that the second-order scattered energy caused by one physical parameter also generates artifacts in the estimations of other physical parameters. Figure 15i–15l shows the inverted model perturbations for elastic constants of c_{33}, c_{55}, c_{11}, and c_{13} using GN method. Figure 15m–15p shows the inverted model perturbations for the elastic constants using FN method after five iterations when model perturbation δc_{33} is 30%. For GN method, the elastic constants c_{33} and c_{55} can be determined very well (Figure 15i and 15j). However, for c_{11} and c_{13} (Figure 15k and 15l), we can still observe some unwanted artifacts, which are caused by the second-order scattered energy in the data residuals due to δc_{33} and δc_{55}. The FN method incorporates the second-order term in the multi-parameter full Hessian for preconditioning. The artifacts in the estimated model perturbations δc_{11} and δc_{13} (Figure 15o and 15p) have been mitigated.

Applying GN and FN multiparameter FWI on a two-block-layer model

Finally, we apply the GN and FN multiparameter FWI on a two-block-layer model for comparison. The model consists of 50×50 grid points with $\Delta x = \Delta z = 10$ m, and a 20 Hz Ricker source wavelet is used for forward modeling. The initial model used in this numerical example is elastic and isotropic. The properties of the initial model are consistent with those used in previous numerical examples. We distribute three sources at $\hat{\mathbf{x}}_{s1}$ = (0 m, 0 m, 0 m), $\hat{\mathbf{x}}_{s2}$ = (250 m, 0 m, 0 m), and $\hat{\mathbf{x}}_{s3}$ = (500 m, 0 m, 0 m). In total, 50 receivers are arranged from 10 to 500 m at the top surface with an interval of 10 m. Two anisotropic block layers are embedded in the isotropic background and the true perturbations for elastic constants c_{33}, c_{55}, c_{11}, and c_{13} are shown in Figure 16a–16d. For the first block layer, the perturbations for elastic constants c_{33}, c_{55}, c_{11}, and c_{13} are -4.218 GPa (-30%), -0.632 GPa (-10%), -1.406 GPa (-10%), and 0 GPa (0%). For the second block layer, the perturbations for these elastic constants are $+4.218$ GPa ($+30\%$), $+0.632$ GPa ($+10\%$), 0 GPa (0%), and $+0.142$ GPa ($+10\%$). The doubly scattered energy between the two block layers can cause artifacts in the estimated model perturbations. A total of 10 iterations are applied for inversion using GN and FN methods. A multiscale approach is used by increasing the frequency band from [1 Hz, 10 Hz] to [1 Hz, 19 Hz] by 1 Hz every iteration (Pratt and Worthington, 1990; Sirgue and Pratt, 2004). To evaluate the quality of the inversion results, we use the relative least-squares error (RLSE) ε,

$$\varepsilon_n = \frac{\|\mathbf{m}_n - \mathbf{m}_t\|}{\|\mathbf{m}_0 - \mathbf{m}_t\|}, \tag{28}$$

where $\mathbf{m}_0$, $\mathbf{m}_t$, and $\mathbf{m}_n$ indicate the initial model, true model, and the inverted model at nth iteration.

Figure 16e–16h shows the inverted model perturbations for elastic constants c_{33}, c_{55}, c_{11}, and c_{13} using GN multiparameter FWI. We can see that for elastic constants c_{33} and c_{55}, GN method can get acceptable results even though the two block layers are not deblurred very well. While for elastic constants c_{11} and c_{13}, the estimated model perturbations are contaminated by strong artifacts. Figure 16i–16l shows the inverted model perturbations for these elastic constants using FN multiparameter FWI. It can be observed that the two block layers for c_{33} are deblurred better and the artifacts for elastic constants c_{11} and c_{13} have been suppressed. Figure 17a–17d shows the RLSE (equation 28) ε_{33}, ε_{55}, ε_{11}, and ε_{13} for elastic constants c_{33}, c_{55}, c_{11}, and c_{13} as the iteration proceeds. The solid lines and dashed lines indicate that the RLSE obtained using GN and FN methods. FN method can estimate the model perturbations more efficiently than GN method by incorporating the second-order term in multiparameter Hessian. Furthermore, Figure 17c and 17d

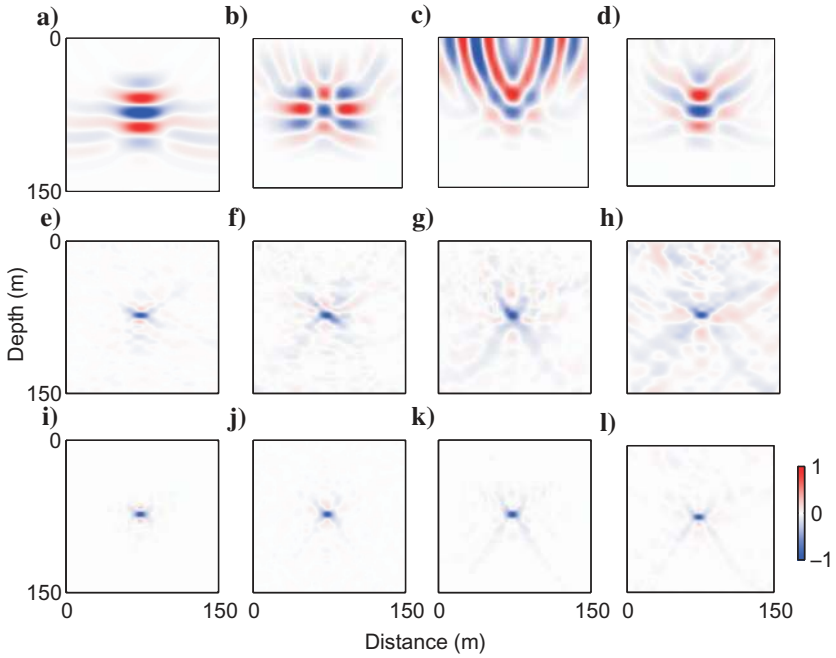

Figure 12. Panels (a-d) show the gradient vectors $\nabla_{c_{33}}\Phi$, $\nabla_{c_{55}}\Phi$, $\nabla_{c_{11}}\Phi$, and $\nabla_{c_{13}}\Phi$ constructed by $\Delta\mathbf{d}$ using three sources. Panels (e-h) show the perturbation estimations with multiparameter approximate Hessian preconditioning for the corresponding elastic constants. Panels (i-l) show the estimated perturbations for elastic constants after three iterations. The amplitudes have been normalized.

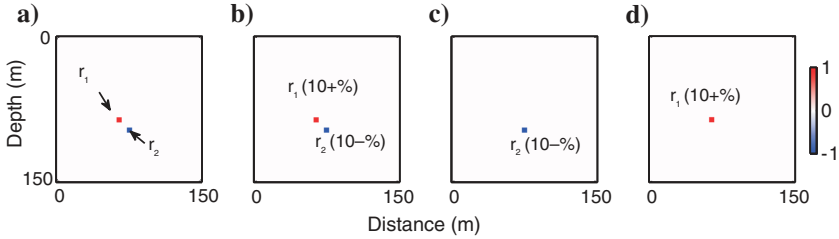

Figure 13. True model perturbations of the two scatterers model. Panels (a-d) show the true model perturbations for elastic constants c_{33}, c_{55}, c_{11}, and c_{13}, respectively. The amplitudes have been normalized.

reveal that the effectiveness of FN method is more obvious in estimating elastic constants c_{11} and c_{13}.

DISCUSSION

We have developed techniques of inversion for the properties of naturally fractured reservoirs using FWI. Robust technology of this kind is expected to have a significant impact in areas like reservoir characterization. Fractured reservoirs can be described using many different parameters, such as fracture spacing, fracture density, fracture orientation, weakness, compliance, etc. Our current study focuses on inverting for the elastic constants of equivalent HTI media. Different parameterizations impact the inversion process greatly, in large part because of parameter crosstalk. Comparison of the stability and efficiency given different parameterizations is an important area of future research. In this paper, we have ignored the contribution from density, which is also very important for characterizing the fluid-filled reservoirs. The 3D scattering patterns for elastic constants in general anisotropic media given in this paper can be used to analyze the parameter crosstalk problem when inverting for the elastic constants. These can subsequently be transformed to any parameterization following the chain rule. The analytic 3D scattering patterns have been examined using a 2D HTI numerical example. Three-dimensional examples for more complex media (such as orthorhombic media) can be carried out in future studies. We ignore the detailed spatial features of the fractured reservoirs by using the long-wavelength approximation and describe the fractured media using anisotropic elastic constants. It will be valuable to consider the fracture size when using FWI for fractured reservoir characterization (Fang et al., 2013; Pan and Innanen, 2013; Zheng et al., 2013).

FWI is an ill-posed problem, which means that an infinite number of models matches the data (Virieux and Operto, 2009). A regularization technique can alleviate the nonuniqueness of the ill-posed inverse problem and make FWI better posed (Menke, 1984). In this paper, no regularization technique is used. Hence, for further research, introducing a regularization technique, such as Tikhonov regularization (Asnaashari et al., 2013) and total-variation regularization (Lin, 2015), in the objective function is necessary for improving the performance of the proposed strategies.

Most current inversion strategies for multiparameter FWI are hierarchical methods, with parameterization and acquisition geometry having been selected to mitigate or avoid parameter crosstalk problem. Prieux et al. (2013) consider viscoacoustic multiparameter FWI using the *l*-BFGS (named after Broyden, 1970; Fletcher, 1970; Goldfarb, 1970; and Shanno, 1970) optimization method with simultaneous strategy, compared against a hierarchical strategy. In

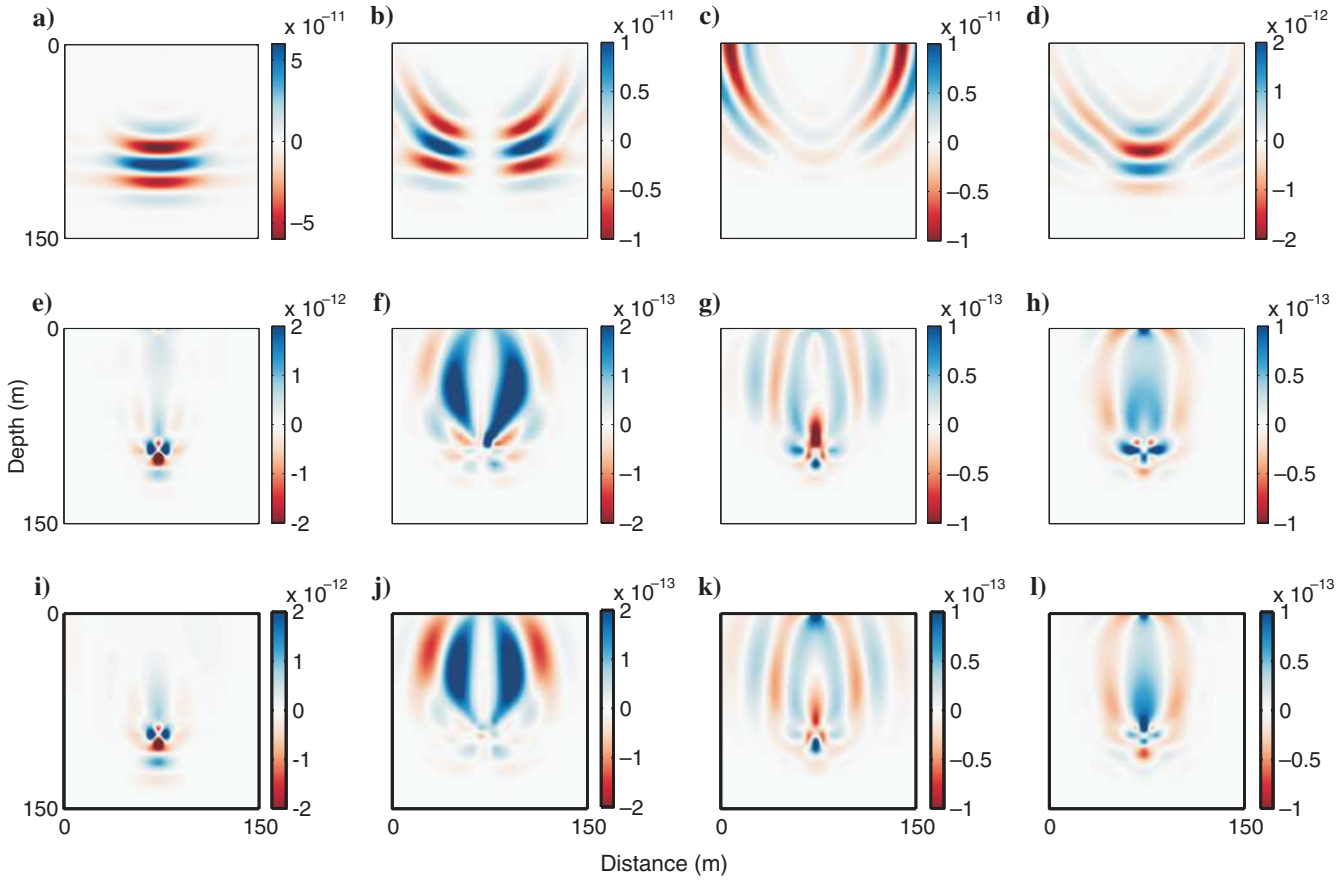

Figure 14. The multiparameter Hessian $\mathbf{H}$ plotted in model space. The green circle in (a) shows parameter position $\mathbf{x}_2$. Panels (a-d) show the 555th rows in the diagonal block $\tilde{\mathbf{H}}_{3333}$ and off-diagonal blocks $\tilde{\mathbf{H}}_{3355}$, $\tilde{\mathbf{H}}_{3311}$, and $\tilde{\mathbf{H}}_{3313}$. Panels (e-h) show the 555th rows in the diagonal block $\tilde{\mathbf{H}}_{3333}$ and off-diagonal blocks $\tilde{\mathbf{H}}_{3355}$, $\tilde{\mathbf{H}}_{3311}$, and $\tilde{\mathbf{H}}_{3313}$. Panels (i-l) show the 555th rows in the blocks $\tilde{\mathbf{H}}_{3333}$, $\tilde{\mathbf{H}}_{3355}$, $\tilde{\mathbf{H}}_{3311}$, and $\tilde{\mathbf{H}}_{3313}$ using adjoint-state method.

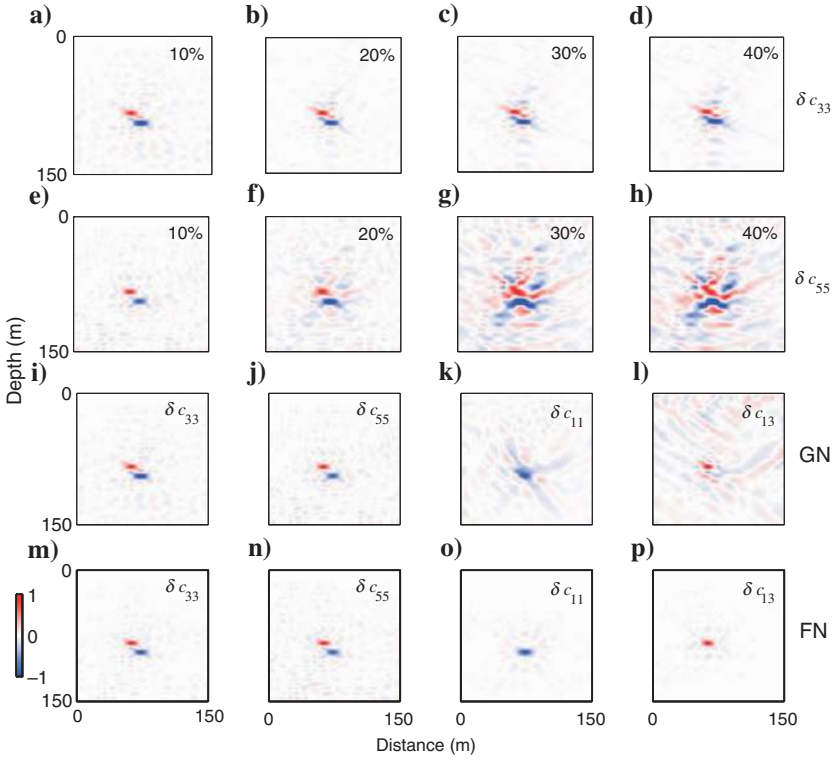

Figure 15. Panels (a-d) show the estimated model perturbation δc_{33} with multiparameter approximate Hessian $\tilde{\mathbf{H}}$ preconditioning when c_{33} is perturbed by 10%, 20%, 30%, and 40%; panels (e-h) show the estimated model perturbation δc_{55} with increasing model perturbations of c_{33}; panels (i-l) show the estimated model perturbations δc_{33}, δc_{55}, δc_{11}, and δc_{11} after five iterations with GN method; panels (m-p) show the estimated model perturbations for the corresponding elastic constants after five iterations with FN method.

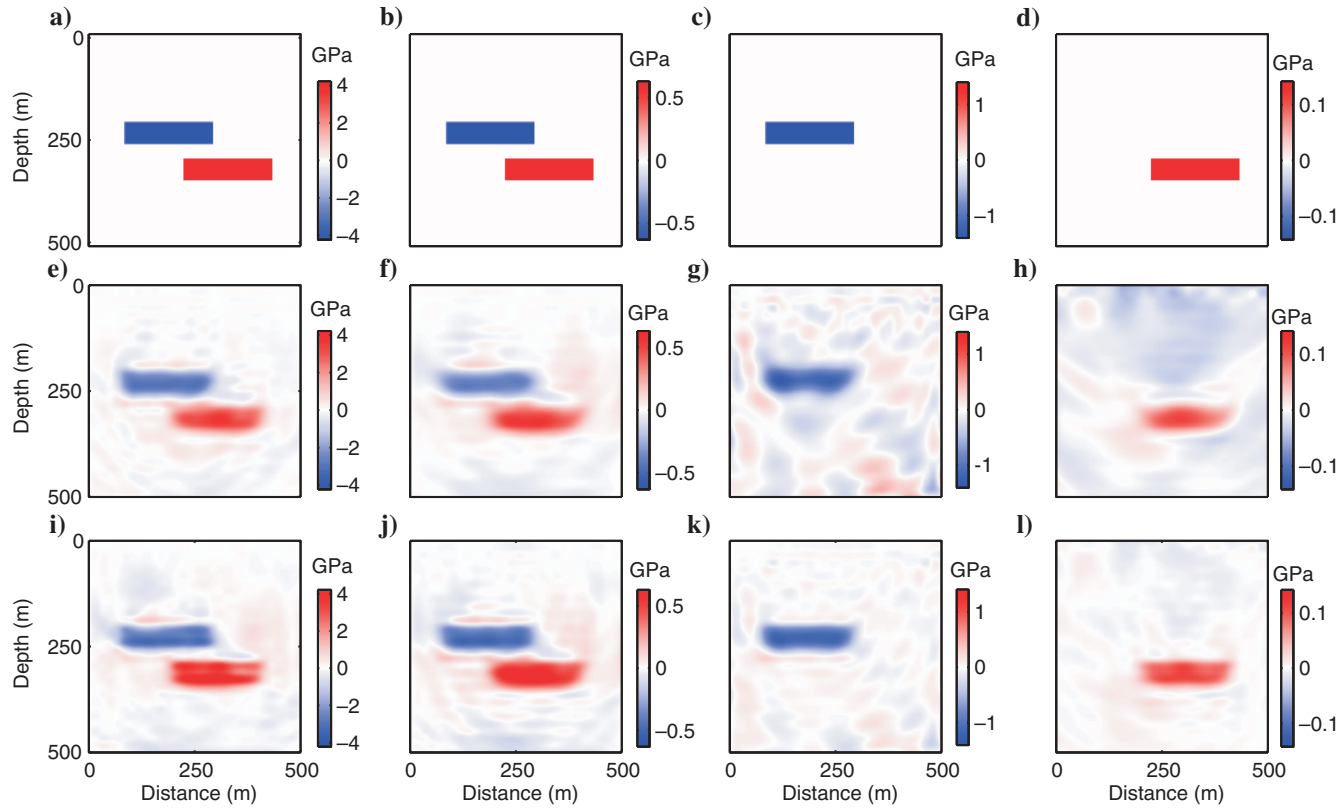

Figure 16. Inversion results comparison. Panels (a-d) show the true model perturbations for the elastic constants c_{33}, c_{55}, c_{11}, and c_{13}, respectively. Panels (e-h) show the inversion results for the elastic constants c_{33}, c_{55}, c_{11}, and c_{13} using GN FWI after 10 iterations. Panels (i-l) show the inversion results for the corresponding elastic constants using FN FWI after 10 iterations.

this paper, to implement the GN and FN methods for estimating elastic constants simultaneously, the multiparameter Hessian matrices are constructed explicitly and then inversed based on SVD. However, these strategies are extremely expensive for large-scale inverse problems. A better choice for large-scale multiparameter FWI is the truncated-Newton method (Métivier et al., 2014, 2015). Instead of constructing the Hessian matrices explicitly, truncated-Newton method only needs Hessian-vector products and obtains the search direction by solving the Newton equation iteratively with CG algorithm.

In the numerical section, we have restricted our selection to 2D numerical examples for examining the possibilities of inverting for the elastic constants. For large 2D or 3D practical applications, it will be much more computationally expensive to carry out GN and FN optimization methods for multiparameter FWI. One possible recourse is target-oriented FWI, in which we only need to calculate one portion of the multiparameter Hessian aiming at the target area. We could potentially also restrict the inverse Hessian construction to the diagonal elements of the off-diagonal blocks, i.e., the parameter-type approximation (Innanen, 2014a) for reducing the computational cost, for which an adjoint-state method would need to be developed. Phase-encoding methods have been widely studied for calculating the gradient (Vigh and Starr, 2008; Tang, 2009; Anagaw and Sacchi, 2014; Pan et al., 2014a) or Hessian approximations (Castellanos et al., 2015). The phase-encoding methods can also be used in multiparameter FWI to calculate the gradient and multiparameter Hessian for reducing the computational burden (Pan et al., 2015a). In this paper, the numerical experiments are used to examine the abilities of multiparameter Hessian, whereas the cycle-skipping difficulty of the inverse problem is ignored. Compared with the quasi-Newton l-BFGS method, GN and FN methods are expected to be more effective for mitigating parameter crosstalk. However, according to Nash (2000), when nonlinearity of the inverse problem becomes very high, the l-BFGS method is more efficient. Hence, an important future step would be to compare the performances of Newton-type methods (GN and FN methods) and l-BFGS method for multiparameter FWI with high nonlinearity.

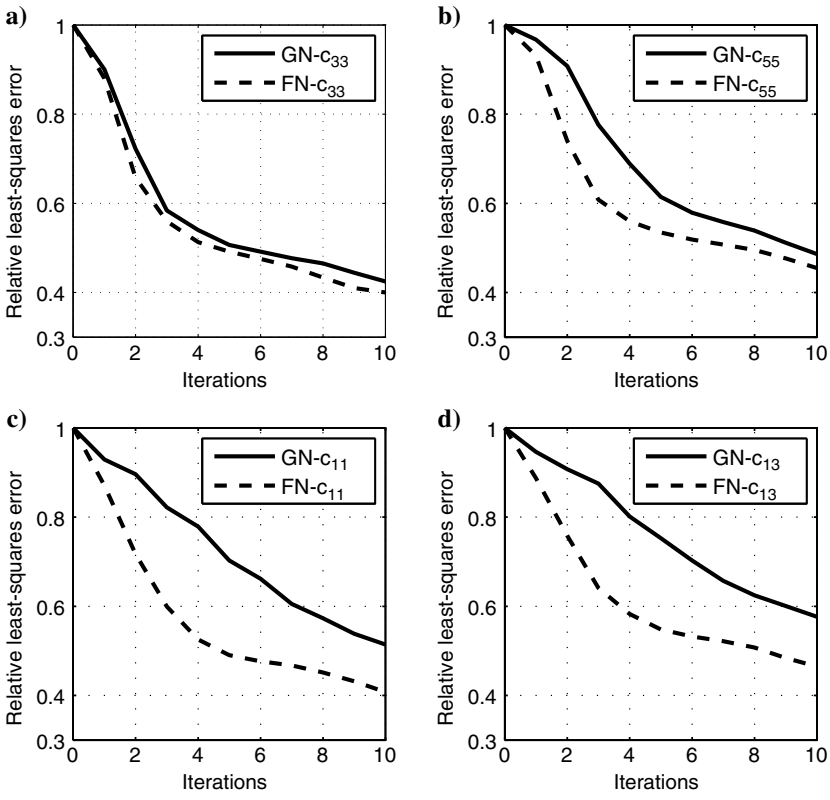

Figure 17. Comparison of the RLSE (equation 28) for different elastic constants using GN and FN methods. Panels (a-d) show the RLSE ε_{33}, ε_{55}, ε_{11}, and ε_{13} for elastic constants c_{33}, c_{55}, c_{11}, and c_{13} as the iteration proceeds.

CONCLUSIONS

In this paper, we have applied the GN and FN multiparameter FWI to invert for the elastic constants of a HTI media. The parameter crosstalk difficulty in multiparameter FWI is introduced, and we also derive the 3D scattering patterns for the elastic constants in general anisotropic media for parameter crosstalk analysis. The role of the multiparameter Hessian in mitigating parameter crosstalk and reducing second-order scattering effects has been revealed. We also explain how to construct the multiparameter second-order preconditioner using the adjoint-state method. In the numerical section, we give examples to testify the effectiveness of the multiparameter Hessian in suppressing parameter crosstalk and second-order scattering effects. The GN and FN FWI are finally applied on a two-block-layer model for comparison. The FN method gave better inversion results for incorporating the multiparameter second-order preconditioner.

ACKNOWLEDGMENTS

This research was supported by the Consortium for Research in Elastic Wave Exploration Seismology (CREWES) and the National Science and Engineering Research Council of Canada (NSERC) (CRDPJ 461179-13). The authors thank researchers D. Yang, S. A. Zamanian, X. Feng, S. Bakku, and S. Brown at MIT-ERL for their valuable discussions and suggestions.

APPENDIX A

3D SCATTERING PATTERNS OF ELASTIC CONSTANTS IN GENERAL ANISOTROPIC MEDIA

The solution of equation 1 can be expressed using the integral form of the Green's tensor vector in the frequency domain (Ben-Menahem and Singh, 1981; Aki and Richards, 2002; Kamath and Tsvankin, 2014):

$$\bar{u}_i(\mathbf{x},\omega) = \int_{\Omega(\mathbf{x}_s)} \int_{\omega_s} f_j(\mathbf{x}_s,\omega_s) G_{ij}(\mathbf{x},\omega;\mathbf{x}_s,\omega_s) d\Omega(\mathbf{x}_s) d\omega_s, \quad \text{(A-1)}$$

where $G_{ij}(\mathbf{x},\omega;\mathbf{x}_s,t_s)$ indicates the ith component of the Green's tensor vector at position $\mathbf{x}$ due to a point source $f_j(\mathbf{x}_s,\omega_s)$ in jth direction at position $\mathbf{x}_s$. The function $\Omega(\mathbf{x}_s)$ indicates the volume including all of the sources.

Considering that a general anisotropic inclusion with density ρ and elastic constants c_{ijkl} is

embedded in an infinite isotropic elastic background with properties $\tilde{\rho}$ and $\tilde{c}_{ijkl}$, the differences between the perturbed and unperturbed model properties are defined as (Stolt and Weglein, 2012)

$$\delta\rho = \rho - \tilde{\rho}, \quad \delta c_{ijkl} = c_{ijkl} - \tilde{c}_{ijkl}, \tag{A-2}$$

where $\delta\rho$ and δc_{ijkl} denote the density and elastic constant perturbations. Assuming that the size of the anisotropic obstacle is rather small compared with the wavelength of the incident wave, the perturbed wavefields corresponding to these model variations can be written as

$$\delta\mathbf{u} = \mathbf{u} - \tilde{\mathbf{u}}, \tag{A-3}$$

where $\tilde{\mathbf{u}}$ and $\delta\mathbf{u}$ indicate the unperturbed wavefields and scattered wavefields, respectively. Plugging equations A-2 and A-3 into equation 1 and ignoring the high-order terms based on the Born approximation, the equation of motion splits into two equations:

$$\frac{\partial}{\partial x_j}\left(\tilde{c}_{ijkl}\frac{\partial \tilde{u}_k}{\partial x_l}\right) - \tilde{\rho}\frac{\partial^2 \tilde{u}_i}{\partial t^2} = -f_i, \tag{A-4}$$

$$\frac{\partial}{\partial x_j}\left(\tilde{c}_{ijkl}\frac{\partial \delta u_k}{\partial x_l}\right) - \tilde{\rho}\frac{\partial^2 \delta u_i}{\partial t^2} = \delta\rho\frac{\partial^2 \tilde{u}_i}{\partial t^2} - \frac{\partial \delta M_{ij}}{\partial x_j}, \tag{A-5}$$

where $\delta\mathbf{M}$ in equation A-5 is the equivalent moment tensor source (Ben-Menahem and Singh, 1981; Chapman, 2004) that indicates the perturbations of the elastic constants:

$$\delta M_{ij} = \delta c_{ijkl}\tilde{e}_{kl}, \tag{A-6}$$

where $\tilde{e}_{kl}$ are the strain components of the incident wave. We notice, first, that equation A-4 is equivalent to equation 1, meaning that the unperturbed wavefield $\tilde{\mathbf{u}}$ propagates in the isotropic background media. Further examination reveals that equation A-5 describes the propagation of the scattered wavefield $\delta\mathbf{u}$ in the isotropic background media. The right side of the equation A-5 is referred to as "scattered sources." It underlines the fact that the scattered wavefields due to the perturbations of the model parameters (e.g., $\delta\rho$ or δc_{ijkl}), can be interpreted as the wavefields generated by a set of secondary body forces, which propagate in the current (or unperturbed) medium (Dietrich and Kormendi, 1990).

According to equation A-1, the solution of equation A-5 can be written as an integral formulation in the frequency domain:

$$\begin{aligned}\delta\bar{u}_n(\mathbf{x},\omega) = &\int_{\Omega(\mathbf{x}')}\int_{\omega'} \delta\rho\omega^2\tilde{u}_i\tilde{G}_{ni}(\mathbf{x},\omega;\mathbf{x}',\omega')d\Omega(\mathbf{x}')d\omega' \\ &+ \int_{\Omega(\mathbf{x}')}\int_{\omega'} \frac{\partial\delta M_{ij}}{\partial x'_j}\tilde{G}_{ni}(\mathbf{x},\omega;\mathbf{x}',\omega')d\Omega(\mathbf{x}')d\omega',\end{aligned} \tag{A-7}$$

where $\tilde{G}_{ij}(\mathbf{x},\omega;\mathbf{x}',\omega')$ indicates the Green's tensor in the unperturbed background medium due to the scattered source at position $\mathbf{x}' = (x', y', z')$. Ignoring the contribution from density (here, we only consider the perturbations of the elastic constants) and applying integration by parts with a far-field approximation, the scattered wavefields can be obtained as

$$\delta\bar{u}_n(\mathbf{x},\omega) \approx -\int_{\Omega(\mathbf{x}')}\int_{\omega'} \delta M_{ij}\frac{\partial\tilde{G}_{ni}(\mathbf{x},\omega;\mathbf{x}',\omega')}{\partial x'_j}d\Omega(\mathbf{x}')d\omega', \tag{A-8}$$

or a more compact form:

$$\delta\bar{u}_n \approx -\delta M_{ij}\tilde{G}_{ni,j}. \tag{A-9}$$

Taking the partial derivative of the scattered wavefields with respect to the variations of the model parameters yields the Fréchet derivative wavefield,

$$\frac{\partial\bar{u}_n(\mathbf{x},\omega)}{\partial\mathbf{m}} = -\int_{\Omega(\mathbf{x}')}\int_{\omega'}\frac{\partial\delta M_{ij}}{\partial\mathbf{m}}\frac{\partial\tilde{G}_{ni}(\mathbf{x},\omega;\mathbf{x}',\omega')}{\partial x'_j}d\Omega(\mathbf{x}')d\omega', \tag{A-10}$$

where $\mathbf{m}$ denotes elastic constants c_{ijkl} in general anisotropic medium. Equation A-10 is known as the Fréchet derivative (or inversion sensitivity kernel) which is widely analyzed and utilized in the linearized inversion framework (Tarantola, 1984, 1986; Pratt et al., 1998; Virieux and Operto, 2009).

Applying Voigt recipe of indexes to the elastic constants perturbation matrix $\delta\mathbf{c}$, equation A-6 can be written in matrix form:

$$\begin{bmatrix}\delta M_{11}\\ \delta M_{22}\\ \delta M_{33}\\ \delta M_{23}\\ \delta M_{13}\\ \delta M_{12}\end{bmatrix} = \begin{bmatrix}\delta c_{11} & \delta c_{12} & \delta c_{13} & \delta c_{14} & \delta c_{15} & \delta c_{16}\\ & \delta c_{22} & \delta c_{23} & \delta c_{24} & \delta c_{25} & \delta c_{26}\\ & & \delta c_{33} & \delta c_{34} & \delta c_{35} & \delta c_{36}\\ & & & \delta c_{44} & \delta c_{45} & \delta c_{46}\\ & & & & \delta c_{55} & \delta c_{56}\\ & & & & & \delta c_{66}\end{bmatrix}\begin{bmatrix}\tilde{e}_{11}\\ \tilde{e}_{22}\\ \tilde{e}_{33}\\ 2\tilde{e}_{23}\\ 2\tilde{e}_{13}\\ 2\tilde{e}_{12}\end{bmatrix}. \tag{A-11}$$

Thus, the information of incident wave is encoded in the equivalent moment tensor source $\delta\mathbf{M}$. First, we can consider an incident plane P-wave,

$$\grave{\mathbf{u}}_p = U\,\mathbf{exp}[i(\omega t - \mathbf{k}_\alpha\cdot\mathbf{n})]\hat{\mathbf{p}}, \tag{A-12}$$

where U is the amplitude of the incident P-wave, "$\cdot$" means inner product, and $\mathbf{n} = (\mathbf{x},\mathbf{y},\mathbf{z})$ indicates the unit vector in Cartesian coordinates. The value $\mathbf{k}_\alpha$ is the P-wave wavenumber vector in Spherical coordinates and $\hat{\mathbf{p}}$ is the polarization vector indicating the positive direction of the particle motion:

$$\mathbf{k}_\alpha = k_\alpha\hat{\mathbf{q}} = k_\alpha(\sin\vartheta\cos\varphi\mathbf{x} + \sin\vartheta\sin\varphi\mathbf{y} + \cos\vartheta\mathbf{z}), \tag{A-13}$$

$$\hat{\mathbf{p}} = \sin\,\vartheta\,\cos\,\varphi\mathbf{x} + \sin\,\vartheta\,\sin\,\varphi\mathbf{y} + \cos\,\vartheta\mathbf{z}, \tag{A-14}$$

where ϑ is the inclination angle of incident wave, which departs from z-axis and φ departing from x-axis indicates the azimuth angle of the incident wave. The value $\hat{\mathbf{q}}$ is the unit vector within spherical coordinates. Thus, the strain components can be obtained as

$$\tilde{e}_{ij} = -ik_\alpha U\hat{p}_i\hat{q}_j\,\mathbf{exp}[i(\omega t - \mathbf{k}_\alpha\cdot\mathbf{n})]. \tag{A-15}$$

Inserting equation A-15 and the analytic expression of the Green's function tensor in 3D isotropic and elastic media (Aki

and Richards, 2002; Chapman, 2004) into equation A-10, we can get the analytic expressions of the 3D Fréchet derivative wavefield with the incident-plane P-wave,

$$\frac{\partial \mathbf{u}_p}{\partial \mathbf{m}} = -\frac{\omega^2 U \exp(-ik_\xi r)}{4\pi\rho\alpha\xi^3 r}(\hat{\mathbf{g}}^\dagger \frac{\partial \mathbb{M}}{\partial \mathbf{m}}\hat{\mathbf{r}}), \tag{A-16}$$

where ξ can be α or β for P-wave velocity or S-wave velocity, respectively. k_ξ can be k_α or k_β for P-wave wavenumber or S-wave wavenumber. The vector $\hat{\mathbf{g}}$ can be $\hat{\mathbf{r}}$, $\hat{\theta}$ and $\hat{\phi}$ for scattered P-wave, SV-wave, and SH-wave:

$$\begin{aligned}\hat{\mathbf{r}} &= [\sin\theta\cos\phi, \sin\theta\sin\phi, \cos\theta]^\dagger,\\ \hat{\theta} &= [\cos\theta\cos\phi, \cos\theta\sin\phi, -\sin\theta]^\dagger\\ \hat{\phi} &= [-\sin\phi, \cos\phi, 0]^\dagger,\end{aligned} \tag{A-17}$$

where θ indicates the inclination angle departing from z-axis and ϕ indicates the azimuth angle departing from x-axis for describing the scattered wave. $\delta\mathbb{M}$ in equation A-16 indicates reduced moment tensor source by taking the terms of $ik_\alpha U$ and $\mathbf{exp}[i(\omega t - \mathbf{k}_\alpha \cdot \mathbf{n})]$ out of $\delta\mathbf{M}$:

$$\delta\mathbf{M} = ik_\alpha U \delta\mathbb{M}\ \mathbf{exp}[i(\omega t - \mathbf{k}_\alpha \cdot \mathbf{n})]. \tag{A-18}$$

In this research, the scattering coefficient (or scattering pattern) due to perturbation of model parameter $\mathbf{m}$ is defined as (Chapman, 2004)

$$\mathbb{R}_p(\vartheta, \varphi, \theta, \phi) = \hat{\mathbf{g}}^\dagger \frac{\partial \mathbb{M}}{\partial \mathbf{m}}\hat{\mathbf{r}}, \tag{A-19}$$

where $\mathbb{R}_p$ is associated with four angles, which are used to describe the incident wave and scattered wave. Similarly, for incident plane SV-wave, we have

$$\grave{\mathbf{u}}_{\mathrm{SV}} = U_{\mathrm{SV}}\,\mathbf{exp}[i(\omega t - \mathbf{k}_\beta \cdot \mathbf{n})]\hat{\mathbf{p}}^{\mathrm{SV}}, \tag{A-20}$$

where U_{SV} is the amplitude of the incident SV-wave, $\mathbf{k}_\beta = k_\beta\hat{\mathbf{q}}$ and $\hat{\mathbf{p}}^{\mathrm{SV}} = \cos\theta\cos\phi\mathbf{x} + \cos\theta\sin\phi\mathbf{y} - \sin\theta\mathbf{z}$. Its strain components can be expressed as

$$\tilde{e}_{ij}^{\mathrm{SV}} = -\tfrac{1}{2}ik_\beta U_{\mathrm{SV}}(\hat{p}_i^{\mathrm{SV}}\hat{q}_j + \hat{p}_j^{\mathrm{SV}}\hat{q}_i)\,\mathbf{exp}[i(\omega t - \mathbf{k}_\beta \cdot \mathbf{n})]. \tag{A-21}$$

For incident plane SH-wave, we have

$$\grave{\mathbf{u}}_{\mathrm{SH}} = U_{\mathrm{SH}}\,\mathbf{exp}[i(\omega t - \mathbf{k}_\beta \cdot \mathbf{n})]\hat{\mathbf{p}}^{\mathrm{SH}}, \tag{A-22}$$

where U_{SH} is the amplitude of incident SH-wave, and $\hat{\mathbf{p}}^{\mathrm{SH}} = -\sin\phi\mathbf{x} + \cos\phi\mathbf{y}$ and its strain components can be expressed as

$$\tilde{e}_{ij}^{\mathrm{SH}} = -\tfrac{1}{2}ik_\beta U(\hat{p}_i^{\mathrm{SH}}\hat{q}_j + \hat{p}_j^{\mathrm{SH}}\hat{q}_i)\mathbf{exp}[i(\omega t - \mathbf{k}_\beta \cdot \mathbf{n})]. \tag{A-23}$$

Inserting the strain components in equations A-21 and A-23 into equation A-11 and then equation A-10, we can obtain the scattered wavefields with incident plane SV-wave and SH-wave:

$$\frac{\partial \mathbf{u}_{\mathrm{SV}}}{\partial \mathbf{m}} = -\frac{\omega^2 U_{\mathrm{SV}}\ \mathbf{exp}(-ik_\xi r)}{4\pi\rho\beta\xi^3 r}\left(\hat{\mathbf{g}}^\dagger \frac{\partial \mathbb{M}^{\mathrm{SV}}}{\partial \mathbf{m}}\hat{\mathbf{r}}\right), \tag{A-24}$$

$$\frac{\partial \mathbf{u}_{\mathrm{SH}}}{\partial \mathbf{m}} = -\frac{\omega^2 U_{\mathrm{SH}}\ \mathbf{exp}(-ik_\xi r)}{4\pi\rho\beta\xi^3 r}\left(\hat{\mathbf{g}}^\dagger \frac{\partial \mathbb{M}^{\mathrm{SH}}}{\partial \mathbf{m}}\hat{\mathbf{r}}\right). \tag{A-25}$$

The scattering patterns given in this research are consistent with the 3D scattering patterns of the isotropic parameters by Wu and Aki (1985).

REFERENCES

Aki, K., and P. G. Richards, 2002, Quantitative seismology, 2nd ed.: University Science Books.

Alkhalifa, T., and R. Plessix, 2014, A recipe for practical full-waveform inversion in anisotropic media: An analytic parameter resolution study: Geophysics, **79**, no. 3, R91–R101, doi: 10.1190/geo2013-0366.1.

Anagaw, A. Y., and M. D. Sacchi, 2014, Comparison of multifrequency selection strategies for simultaneous-source full-waveform inversion: Geophysics, **79**, no. 5, R165–R181, doi: 10.1190/geo2013-0263.1.

Asnaashari, A., R. Brossier, S. Garambois, F. Audebert, P. Thore, and J. Virieux, 2013, Regularized seismic full-waveform inversion with prior model information: Geophysics, **78**, no. 2, R25–R36, doi: 10.1190/geo2012-0104.1.

Baumstein, A., 2014, Extended subspace method for attenuation of crosstalk in multiparameter full wavefield inversion: 84th Annual International Meeting, SEG, Expanded Abstracts, 1121–1125.

Ben-Menahem, A., and S. Singh, 1981, Seismic waves and sources, 2nd ed.: New York.

Berenger, J., 1994, A perfectly matched layer for the absorption of electromagnetic waves: Journal of Computational Physics, **114**, 185–200, doi: 10.1006/jcph.1994.1159.

Broyden, C. G., 1970, The convergence of a class of double-rank minimization algorithms: IMA Journal of Applied Mathematics, **6**, 222–231.

Castellanos, C., L. Métivier, S. Operto, R. Brossier, and J. Virieux, 2015, Fast full waveform inversion with source encoding and second-order optimization methods: Geophysical Journal International, **200**, 718–742, doi: 10.1093/gji/ggu427.

Chapman, C., 2004, Fundamentals of seismic wave propagation: Cambridge University Express.

Crampin, S., 1984, An introduction to wave propagation in anisotropic media: Geophysical Journal International, **76**, 17–28, doi: 10.1111/j.1365-246X.1984.tb05018.x.

Dietrich, M., and F. Kormendi, 1990, Perturbation of plane-wave reflectivity of a depth-dependent elastic medium by weak inhomogeneities: Geophysical Journal International, **100**, 203–214, doi: 10.1111/j.1365-246X.1990.tb02480.x.

Fang, X., M. C. Fehler, T. Chen, D. R. Burns, and Z. Zhu, 2013, Sensitivity analysis of fracture scattering: Geophysics, **78**, no. 1, T1–T10, doi: 10.1190/geo2011-0521.1.

Fichtner, A., and J. Trampert, 2011, Hessian kernels of seismic data functionals based upon adjoint techniques: Geophysical Journal International, **185**, 775–798, doi: 10.1111/gji.2011.185.issue-2.

Fletcher, R., 1970, A new approach to variable metric algorithms: The Computer Journal, **13**, 317–322.

Forgues, E., and G. Lambaré, 1997, Parameterization study for acoustic and elastic ray+Born inversion: Journal of Seismic Exploration, **6**, 253–278.

Gauthier, O., J. Virieux, and A. Tarantola, 1986, Two-dimensional nonlinear inversion of seismic waveforms: Numerical results: Geophysics, **51**, 1387–1403, doi: 10.1190/1.1442188.

Gholami, Y., R. Brossier, S. Operto, V. Prieus, A. Ribodetti, and J. Virieux, 2013a, Which parameterization is suitable for acoustic vertical transverse isotropic full waveform inversion? Part 2: Synthetic and real data case studies from Valhall: Geophysics, **78**, no. 2, R107–R124, doi: 10.1190/geo2012-0203.1.

Gholami, Y., R. Brossier, S. Operto, A. Ribodetti, and J. Virieux, 2013b, Which parametrization for acoustic VTI full waveform inversion? — Part 1: Sensitivity and tradeoff analysis: Geophysics, **78**, no. 2, R81–R105, doi: 10.1190/geo2012-0204.1.

Goldfarb, D., 1970, A family of variable-metric methods derived by variational means: Mathematics of Computation, **24**, 23–26.

Hudson, J. A., 1981, Wave speeds and attenuation of elastic waves in material containing cracks: Geophysical Journal of the Royal Astronomical Society, **64**, 133–150, doi: 10.1111/j.1365-246X.1981.tb02662.x.
Innanen, K. A., 2014a, Reconciling seismic AVO and precritical reflection FWI-analysis of the inverse Hessian: 84th Annual International Meeting, SEG, Expanded Abstracts, 1022–1027.
Innanen, K. A., 2014b, Seismic AVO and the inverse Hessian in precritical reflection full waveform inversion: Geophysical Journal International, **199**, 717–734, doi: 10.1093/gji/ggu291.
Kamath, N., and I. Tsvankin, 2014, Sensitivity analysis for elastic full-waveform inversion in VTI media: 84th Annual International Meeting, SEG, Expanded Abstracts, 1162–1166.
Lailly, P., 1983, The seismic inverse problem as a sequence of before stack migration: Conference on Inverse Scattering, Theory and Applications, SIAM, Expanded Abstracts, 206–220.
Levander, A. R., 1988, Fourth-order finite-difference P-SV seismograms: Geophysics, **53**, 1425–1436, doi: 10.1190/1.1442422.
Lin, Y., 2015, Acoustic- and elastic-waveform inversion using a modified total-variation regularization scheme: Geophysical Journal International, 502–489 ,**200**, doi: 10.1093/gji/ggu393.
Ma, Y., and D. Hale, 2012, Quasi-Newton full-waveform inversion with a projected Hessian matrix: Geophysics, **77**, no. 5, R207–R216, doi: 10.1190/geo2011-0519.1.
Marfurt, K., 1984, Accuracy of finite-difference and finite-elements modeling of the scalar and elastic wave equation: Geophysics, **49**, 533–549, doi: 10.1190/1.1441689.
Menke, W., 1984, Geophysical data analysis: Discrete inverse theory: Academic Press.
Métivier, L., F. Bretaudeau, R. Brossier, J. Virieux, and S. Operto, 2014, Full waveform inversion and the truncated Newton method: Quantitative imaging of complex subsurface structures: Geophysical Prospecting, **62**, 1–16, doi: 10.1111/gpr.2014.62.issue-1.
Métivier, L., R. Brossier, S. Operto, and J. Virieux, 2015, Acoustic multiparameter FWI for the reconstruction of P-wave velocity, density and attenuation: Preconditioned truncated Newton approach: 85th Annual International Meeting, SEG, Expanded Abstracts, 1198–1203.
Métivier, L., R. Brossier, J. Virieux, and S. Operto, 2013, Full waveform inversion and the truncated Newton method: SIAM Journal On Scientific Computing, **35**, B401–B437, doi: 10.1137/120877854.
Nash, S. G., 2000, A survey of truncated-Newton methods: Journal of computational and applied mathematics, **124**, 45–59, doi: 10.1016/S0377-0427(00)00426-X.
Nelson, R. A., 1985, Geologic analysis of naturally fractured reservoirs, 2nd ed.: Golf Professional Publishing.
Nocedal, J., and S. J. Wright, 2006, Numerical optimization: Springer.
Oh, J., T. Alkhalifah, and D. Min, 2015, Multi-stage full waveform inversion strategy for 2D elastic VTI media: 85th Annual International Meeting, SEG, Expanded Abstracts, 1204–1208.
Operto, S., Y. Gholami, V. Prieux, A. Ribodetti, R. Brossier, L. Metivier, and J. Virieux, 2013, A guided tour of multiparameter full waveform inversion with multicomponent data: From theory to practice: The Leading Edge, **32**, 1040–1054, doi: 10.1190/tle32091040.1.
Pan, W., and K. A. Innanen, 2013, AVO/AVF analysis of thin beds in elastic media: 83rd Annual International Meeting, SEG, Expanded Abstracts, 373–377, doi: 10.1190/segam2013-0587.1.
Pan, W., K. A. Innanen, and G. F. Margrave, 2014a, A comparison of different scaling methods for least-squares migration/inversion: 76th Annual International Conference and Exhibition, EAGE, Extended Abstracts, doi: 10.3997/2214-4609.20141164.
Pan, W., K. A. Innanen, and G. F. Margrave, 2014b, Efficient full waveform inversion in the time-ray parameter domain using iteration-dependent sets of ray parameters: CPS/SEG Technical Program Expanded Abstracts, doi: 10.1190/IGCBeijing2014-198.
Pan, W., K. A. Innanen, G. F. Margrave, and D. Cao, 2015a, Efficient pseudo-Gauss-Newton full-waveform inversion in the τ –p domain: Geophysics, **80**, no. 5, R225–R14, doi: 10.1190/geo2014-0224.1.
Pan, W., K. A. Innanen, G. F. Margrave, M. C. Fhler, X. Fang, and J. Li, 2015b, Estimation of elastic constants in HTI media using Gauss-Newton and Full-Newton multi-parameter full waveform inversion: 85th Annual International Meeting, SEG, Expanded Abstracts, 1177–1182, doi: 10.1190/segam2015-5829154.1.
Pan, W., G. F. Margrave, and K. A. Innanen, 2014c, Iterative modeling migration and inversion (IMMI): Combining full waveform inversion with standard inversion methodology: 84th Annual International Meeting, SEG, Expanded Abstracts, 938–943, doi: 10.1190/segam2014-0402.1.
Pica, A., J. P. Diet, and A. Tarantola, 1990, Nonlinear inversion of seismic reflection data in a laterally invariant medium: Geophysics, **55**, 284–292, doi: 10.1190/1.1442836.
Plessix, R. E., 2006, A review of the adjoint-state method for computing the gradient of a functional with geophysical applications: Geophysical Journal International, **167**, 495–503, doi: 10.1111/gji.2006.167.issue-2.
Podgornova, O., S. Leaney, and L. Liang, 2015, Analysis of resolution limits of VTI anisotropy with full waveform inversion: 85th Annual International Meeting, SEG, Expanded Abstracts, 1188–1192.
Pratt, R. G., C. Shin, and G. J. Hicks, 1998, Gauss-Newton and full Newton methods in frequency-space seismic waveform inversion: Geophysical Journal International, **133**, 341–362, doi: 10.1046/j.1365-246X.1998.00498.x.
Pratt, R. G., and M. H. Worthington, 1990, Inverse theory applied to multi-source crosshole tomography. Part I: Acoustic wave-equation method: Geophysical Prospecting, **38**, 287–310, doi: 10.1111/gpr.1990.38.issue-3.
Prieux, V., R. Brossier, S. Operto, and J. Virieux, 2013, Multiparameter full waveform inversion of multicomponent ocean-bottom cable data from the Valhall field. Part 1: Imaging compressional wave speed, density and attenuation: Geophysical Journal International, **194**, 1640–1664, doi: 10.1093/gji/ggt177.
Rüger, A., 1997, P-wave reflection coefficients for transversely isotropic models with vertical and horizontal axis of symmetry: Geophysics, **62**, 713–722, doi: 10.1190/1.1444181.
Schoenberg, M., 1983, Reflection of elastic waves from periodically stratified media with interfacial slip: Geophysical Prospecting, **31**, 265–292, doi: 10.1111/gpr.1983.31.issue-2.
Shanno, D. F., 1970, Conditioning of quasi-Newton methods for function minimization: Mathematics of Computation, **24**, 647–656.
Shin, C., K. Yoon, K. J. Marfurt, K. Park, D. Yang, H. Y. Lim, S. Chung, and S. Shin, 2001, Efficient calculation of a partial-derivative wavefield using reciprocity for seismic imaging and inversion: Geophysics, **66**, 1856–1863, doi: 10.1190/1.1487129.
Sirgue, L., and R. G. Pratt, 2004, Efficient waveform inversion and imaging: A strategy for selecting temporal frequencies: Geophysics, **69**, 231–248, doi: 10.1190/1.1649391.
Stolt, R. H., and A. B. Weglein, 2012, Seismic imaging and inversion: Application of linear inverse theory: Cambridge University Press.
Tang, Y., 2009, Target-oriented wave-equation least-squares migration/inversion with phase-encoded Hessian: Geophysics, **74**, no. 6, WCA95–WCA107, doi: 10.1190/1.3204768.
Tarantola, A., 1984, Inversion of seismic reflection data in the acoustic approximation: Geophysics, **49**, 1259–1266, doi: 10.1190/1.1441754.
Tarantola, A., 1986, A strategy for nonlinear elastic inversion of seismic reflection data: Geophysics, **51**, 1893–1903, doi: 10.1190/1.1442046.
Thomsen, L., 1988, Reflection seismology over azimuthally anisotropic media: Geophysics, **53**, 304–313, doi: 10.1190/1.1442464.
Tromp, J., C. Tape, and Q. Liu, 2005, Seismic tomography, adjoint methods, time reversal, and banana-doughnut kernels: Geophysical Journal International, **160**, 195–216, doi: 10.1111/gji.2005.160.issue-1.
Tsvankin, I., 1997a, Anisotropic parameters and P-wave velocity for orthorhombic media: Geophysics, **62**, 1292–1309, doi: 10.1190/1.1444231.
Tsvankin, I., 1997b, Reflection moveout and parameter estimation for horizontal transverse isotropy: Geophysics, **62**, 614–629, doi: 10.1190/1.1444170.
Tsvankin, I., and V. Grechka, 2011, Seismology of azimuthally anisotropic media and seismic fracture characterization: SEG.
Valenciano, A., 2008, Imaging by wave-equation inversion: Ph.D. thesis, Stanford University.
Vigh, D., and E. W. Starr, 2008, 3D prestack plane-wave, full-waveform inversion: Geophysics, **73**, no. 5, VE135–VE144, doi: 10.1190/1.2952623.
Virieux, J., 1986, P-SV wave propagation in heterogeneous media: Geophysics, **51**, 889–901, doi: 10.1190/1.1442147.
Virieux, A., and S. Operto, 2009, An overview of full-waveform inversion in exploration geophysics: Geophysics, **74**, no. 6, WCC1–WCC26, doi: 10.1190/1.3238367.
Wang, T., and X. Tang, 2003, Finite-difference modeling of elastic wave propagation: A nonsplitting perfectly matched layer approach: Geophysics, **68**, 1749–1755, doi: 10.1190/1.1620648.
Warner, M., and L. Guasch, 2014, Adaptive waveform inversion: Theory: 84th Annual International Meeting, SEG, Expanded Abstracts, 1089–1093.
Warner, M., A. Ratclie, T. Nangoo, J. Morgan, A. Umpleby, N. Shah, V. Vinje, I. Stekl, L. Guasch, C. Win, G. Conroy, and A. Bertrand, 2013, Anisotropic 3D full-waveform inversion: Geophysics, **78**, no. 2, R59–R80, doi: 10.1190/geo2012-0338.1.
Wu, R., and K. Aki, 1985, Scattering characteristics of elastic waves by an elastic heterogeneity: Geophysics, **50**, 582–595, doi: 10.1190/1.1441934.
Wu, W., J. Luo, and B. Wu, 2014, Seismic envelope inversion and modulation signal model: Geophysics, **79**, no. 3, WA13–WA24, doi: 10.1190/geo2013-0294.1.
Zheng, Y., X. Fang, M. C. Fehler, and D. R. Burns, 2013, Seismic characterization of fractured reservoirs by focusing Gaussian beams: Geophysics, **78**, no. 4, A23–A28, doi: 10.1190/geo2012-0512.1.